geosciences

MDPI

Review

Estimating Earthquake-Induced Pore Water Pressure: Hierarchy of Existing Methods

Anna Chiaradonna

Department of Civil, Construction-Architectural and Environmental Engineering, University of L'Aquila, Piazzale E. Pontieri 1, Monteluco di Roio, 67100 L'Aquila, Italy; anna.chiaradonna1@univaq.it; Tel.: +39-0862-4507

Abstract

The prediction of earthquake-induced excess pore water pressure is becoming a crucial step for liquefaction-related problems, such as the prediction of settlements, assessment of bearing capacity of shallow foundations, and efficiency of liquefaction mitigation measurements. The goal of this review is to provide a state of the art of the available methods for estimating excess pore water pressure from the most simplified approaches, based on simple hand-made calculations, to the most simplified models for pore pressure prediction, and finally to the most advanced models implemented in computer codes for seismic site response analysis. The hierarchy of the methods is enriched with exemplificative applications from real cases to help understand the classification provided and the usability of each method according to the needs of the professional practice.

Keywords: pore water pressure; earthquake; safety factor against liquefaction; simplified dynamic analysis; stress-based pore pressure model; loosely coupled; fully coupled; effective stress non-linear dynamic analysis; advanced constitutive model

1. Introduction

Seismically induced excess pore water pressure within saturated loose sandy soils is fundamentally triggered by cyclic loadings under undrained conditions. This reduces the soil effective stress state by activating a mechanism that can culminate in either catastrophic flow failure (liquefaction) or progressive strain degradation (cyclic softening).

Experimental research assessed that the generation of excess pore water pressure depends strongly on ground motion parameters (e.g., peak ground acceleration—PGA, duration, frequency content), with high correlation with PGA and Arias Intensity [1]. Kamura et al. [2] show results from continuously measuring ground acceleration and pore water pressure at a liquefaction-prone site in Japan. Based on the records, they established a threshold acceleration value that initiates the triggering of excess pore pressure and defined the "contribution duration" as the temporal interval during which the recorded ground motion accelerations surpassed the established threshold.

An investigation performed in a laboratory on layered sand columns showed that soil type, density, and layering/permeability contrasts significantly affect the dissipation rates and attained values of the pore pressure build-up, where lower permeability interlayers prolong high excess pore water pressure [3]. Large-scale shaking table model tests and centrifuge tests also confirm that initial liquefaction onset and pore water pressure evolution depend on seismic intensity and soil stratigraphy [4,5].

Experiments investigating the mechanisms of excess pore water pressure generation with a structure settled on soil deposits and without (free-field) show the complexity of

Check for updates

Academic Editors: Salvatore Grasso and Ioannis Koukouvelas

Received: 3 November 2025
Revised: 15 January 2026
Accepted: 24 January 2026
Published: 1 February 2026

Copyright: © 2026 by the author. Licensee MDPI, Basel, Switzerland. This article is an open access article distributed under the terms and conditions of the Creative Commons Attribution (CC BY) license.

the problem depending on the type and geometry of the foundations and soil properties and the layering configurations [6–11]. Due to their complexity, the effects of buildings on pore pressure generation are beyond the scope of this review. In addition, after excess pore pressure build-up, the dissipation and reconsolidation process controls post-earthquake deformation and settlements, with permeability and void ratio evolution playing a key role in reconsolidation behavior [12–17].

Cubrinovski et al. [18] demonstrated via effective stress dynamic analysis that the simple metrics (like CPT-based assessment) for the critical layers were essentially identical between sites that experienced liquefaction and sites that experienced no liquefaction after the 2010–2011 Canterbury seismic events, implying the urgency to consider the entire soil profile behavior (i.e., the "system response") rather than just the properties of the individual weakest layer.

For the above reason, the prediction of the seismically induced excess pore water pressure is of utmost importance.

Machine learning approaches are emerging to predict excess pore water pressure response from stress histories and soil properties [19]. Since this is an emerging research area, it was also beyond the scope of this review.

Biondi [20] reviews in detail several pore water pressure relationships by classifying them into two different groups: the first encompasses empirical relationships which are formulated as analytical functions to replicate the outcomes of experimental testing, e.g., [21–27]; the second one includes relations derived from theoretical models of the cyclic soil behavior, with experimental data used for parameter calibration, e.g., [28–30].

One of the most popular analytical relationships belonging to the first group has been proposed by Booker et al. [31] as follows:

$$r_u = \frac{2}{\pi}\arcsin\left(\frac{N}{N_L}\right)^{1/2\beta} \quad (1)$$

where r_u is the pore pressure ratio defined as the ratio between the seismically induced pore pressure increment, Δu, and the initial effective overburden stress, σ'_{v0}, N is the number of cycles, N_L is the number of cycles to reach liquefaction, and β is a coefficient depending on and physical and mechanical soil properties.

Several modified versions of the above Equation (1) were proposed to better fit the test data; such as in a recent publication [32].

In such a way, N/N_L can be considered a factor of safety because it correlates with the seismic demand, N, and the soil resistance to liquefaction, N_L.

The use of the first group identified by Biondi [20] typically necessitates a comparison between the irregular loading due to an earthquake and the soil resistance as determined from laboratory investigations, which commonly employ uniform loads. To make this comparison possible, the irregular shaking must first be converted into an equivalent series of uniform cycles. Following the pioneering studies by Seed et al. [33], a shear stress history variable at any given time due to the earthquake can be reduced into an equivalent number of cycles, N_{eq}, with amplitude equal to 0.65 of the maximum shear stress, τ_{max}, which would cumulatively produce the same excess pore pressure buildup as the actual motion. A significant number of methodologies have been developed to estimate the equivalent number of uniform cycles of an earthquake (e.g., [34–37]). However, these approaches are often not easy to apply, and the results are highly dependent on the conversion criterion and the techniques used for selecting and counting the cycles that contribute to pore pressure accumulation [38].

Hashash et al. [39] classified the pore pressure generation models into three categories: stress-based, strain-based, and energy-based models, based on the variable used for pre-

dicting the pore pressure build-up (i.e., shear stress, shear strain, or dissipated energy, respectively). Hashash et al. [39] observed that if the cyclic stress-controlled tests inspired the stress-based approach, other subsequent research proposed a correlation with the shear strain [40,41] or the energy dissipated within the soil deposit [42].

In the strain-based pore pressure models, Chen et al. [43] proposed a model where residual excess pore water pressure is quantified by the volumetric strain changes owing to cyclic shearing, accounting for the concept of threshold shear strain, i.e., the strain below which excess pressure is not generated.

In the framework of the stress-based pore pressure models, excess pore water pressure can be estimated in a simplified manner based on the damage parameter as proposed by Chiaradonna et al. [44,45]. This model utilizes a defined damage parameter, κ, which is an incrementing variable throughout the loading history and establishes a direct correlation with the pore pressure accumulation according to the following relationship:

$$r_u = a\left(\frac{\kappa}{\kappa_L}\right)^b + c\left(\frac{\kappa}{\kappa_L}\right)^d \quad (2)$$

where a, b, c, and d are fitted model parameters, and κ_L is the damage parameter at liquefaction, defined as follows:

$$\kappa_L = 4\, N_r (CSR_r - CSR_t)^{\alpha} \quad (3)$$

where (N_r, CSR_r) identifies a reference point, CSR_t is the threshold below which there is no pore pressure accumulation, and the parameter α defines the dependency of the soil resistance on the number of cycles. This latter is analytically described as a relationship proposed by Park et al. [46]:

$$\frac{(CRR - CSR_t)}{(CSR_r - CSR_t)} = \left(\frac{N_r}{N_L}\right)^{\frac{1}{\alpha}} \quad (4)$$

Due to the proportionality between the damage parameter and the number of cycles for uniform cyclic loading [45], Equation (2) can be rewritten as follows:

$$r_u = a\left(\frac{N}{N_L}\right)^b + (0.95 - a)\left(\frac{N}{N_L}\right)^d \quad (5)$$

where N/N_L is the same normalized number of cycles as Equation (1).

For a generic history of shear stress, this is normalized to the initial vertical effective stress as follows:

$$\tau^*(t) = \frac{|\tau(t)|}{\sigma'_{v0}} \quad (6)$$

For a time instant, the damage parameter is computed as follows:

$$\kappa(t) = \kappa_0 + d\kappa \quad (7)$$

where κ_0 is the damage cumulated at the last reversal point of the function (τ^*, CSR_t) reached at the time instant, t. The damage κ_0 is defined as follows:

$$\kappa_0 = \begin{cases} \kappa(t - dt) & \text{if } \dot{\tau}^*(t) = 0 \quad \text{or } \tau^*(t) = CSR_t \\ \kappa_0(t - dt) & \text{if } \dot{\tau}^*(t) \neq 0 \quad \text{or } \tau^*(t) \neq CSR_t \end{cases} \quad (8)$$

i.e., κ_0 is a stepwise function assuming the value of the damage parameter gained at the time step ($t - dt$) every time the stress ratio is a local maximum or when $\tau^* = CSR_t$.

The increment of the damage parameter, $d\kappa$, in the time interval dt is as follows:

$$d\kappa = \begin{cases} 0 & \text{if } \tau^*(t) < CSR_t \\ [\tau_0^*(t) - \tau(t)]^{\alpha} & \text{if } \tau^*(t) \geq CSR_t \end{cases} \quad (9)$$

The accumulation of damage occurs every time τ^* overtakes CSR_t.

This simplified model avoids converting the irregular stress history into an equivalent number of cycles and it can be used to predict the pore pressure ratio time history for any type of loading after the calibration of the pore water pressure—PWP—model parameters (a, b, c, and d of Equation (5) and CSR_t, N_r, CSR_r, and α of Equation (4)). Further details on the PWP model and calibration procedure can be found in Chiaradonna et al. [45,47].

If the pore pressure generation models can only predict the residual component of the excess pore pressure generated in saturated soil during cyclic loading, advanced constitutive models working in effective stress (e.g., [48–51]) can correctly predict both transient and residual components of the excess pore water pressure [52,53]. The first component has little influence on soil behavior under saturated conditions because it equalizes the variation of the applied mean normal stresses arising from the cyclic loading [54,55]. The residual component has a predominant impact on the soil strength and stiffness because it is the result of plastic strain of the soil skeleton [42,56].

The effective stress models necessitate several input data to accurately characterize the response of granular soils subjected to elastic or elastoplastic deformations. Furthermore, they must capture common features observed in soils susceptible to liquefaction, specifically the following: the volumetric strain accumulation under cyclic loading, dilatancy at large shear strains, and the effect of fabric history on dilatancy [57].

This review aims to pragmatically provide a classification from the point of view of the possible applicative methods in professional practice. The novelty of the proposed hierarchy is the categorization based on both the complexity and the level of accuracy of the performed analysis in view of practical applications. The following Section 2 describes the predictive approaches graded with an increasing level of complexity (synthetic, simplified, approximate, and rigorous), while the following sections focus on each level. Then, all the methods are applied to an Italian case study and critically discussed in Section 7. Further exemplificative applications are reported in Appendix A. Supplementary Materials also include example spreadsheets to support the application of the most popular methods. Limits and benefits are listed for each method, finally giving a guide for selecting the most suitable one according to the relevance of the problem and requested resources.

2. Hierarchy of Approaches for Excess Pore Water Pressure Prediction

The prediction of the accumulation of excess pore water pressure induced by seismic loading can be assessed with two possible approaches (Figure 1):

1. 'Decoupled' approach, where the computation of excess pore pressure is performed after the end of the calculations, i.e., hand-made calculations of the safety factor against liquefaction or ground response analysis in total stress (e.g., [58]). In both cases, the seismic demand used in the calculations does not account for the generation of pore water pressure.
2. 'Coupled' approach, which consists of non-linear dynamic analyses in effective stress by using either a simplified or an advanced soil constitutive model [39,59]. In this second case, the seismic demand used in the calculation of the excess pore water time history is progressively affected by pore pressure generation.

Within the framework of the 'decoupled' approach, two distinct methods with increasing complexity can be identified (Figure 1):

1.1. 'Synthetic' methods can provide an overall estimate of the expected pore pressure build-up, independently of time;
1.2. 'Simplified' methods are able to provide the history of the excess pore pressure by adopting one of the pore pressure generation models, such as reported by Hashash et al. [39]. This method can be adopted after the execution of total stress ground response analysis.

Within the framework of the 'coupled' approach, two distinctions can be drawn in terms of complexity of the method and analysis level, respectively (Figure 1):

2.1. 'Approximate' methods or 'loosely coupled' analyses that can predict pore pressures by utilizing pore pressure generation models in conjunction with cyclic response models formulated in total stress [60,61]. The crucial aspect that guarantees the coupling between the previous two ingredients of the analysis is the adoption of a degradation model, i.e., how the generated pore pressure models affect the cyclic soil response. The most common degradation models have been proposed by [62].
2.2. 'Rigorous' methods or 'fully coupled' analyses that employ advanced soil constitutive models that are intrinsically formulated within the effective stress framework. These models simultaneously and fully predict both the stress–strain response and the pore pressure response of the soil, addressing the coupled nature of the soil skeleton and pore–fluid interaction [63–65].

Figure 1 graphically summarizes the discussed classification.

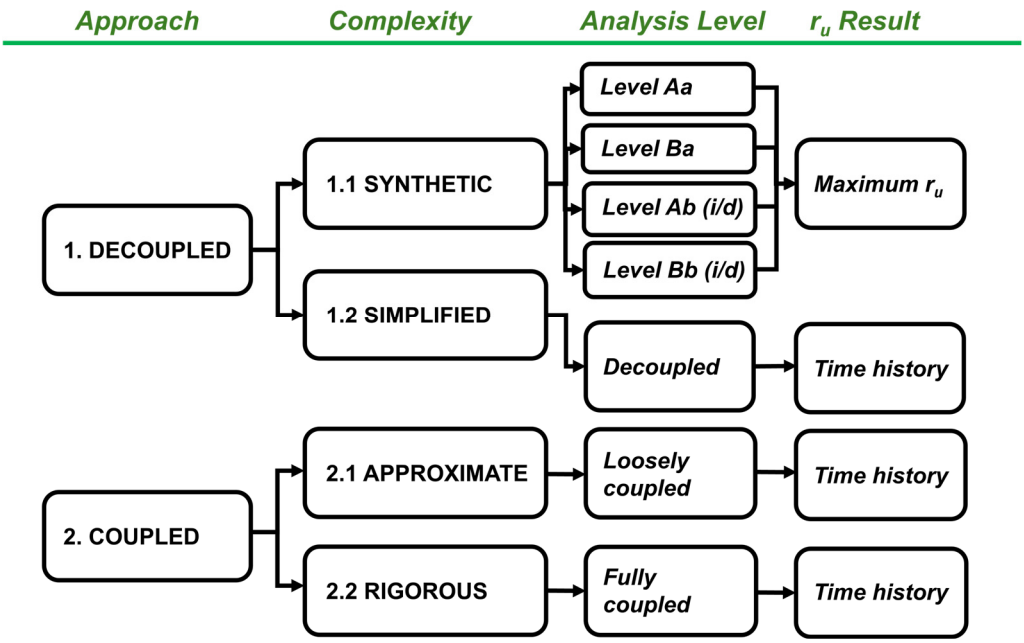


Figure 1. Hierarchy of existing approaches for pore water pressure accumulation.

3. Synthetic Methods

The 'synthetic' methods provide an overall estimate of the maximum expected pore pressure build-up, i.e., just a single value of r_u, independent of the time of attainment (Figure 1). This type of prediction can be adopted after the calculation of the safety factor against liquefaction. Theoretically, the safety factor against liquefaction can be computed according to different approaches, again classified as stress-based, strain-based, and energy-based depending on whether the seismic demand and soil resistance are quantified in terms of normalized stress, strain, or dissipated energy, respectively. However, since the

stress-based approach is the most popular and universally accepted one, it will be referred to in the following.

According to the stress-based procedure [66], the factor of safety (FS) is calculated as the ratio between the cyclic resistance ratio (CRR) of the soil and the seismic demand induced by the earthquake, called the cyclic stress ratio (CSR), both referring to the same conditions (e.g., effective stress confinement, magnitude of the seismic scenario, and so on). All the details can be easily found in the literature [67–70].

Although easy to use, Olson et al. [71] identified three main limitations in this approach: (1) application of several correction factors, e.g., the depth reduction, magnitude scaling, and overburden correction factors; (2) the use of a total stress framework to describe the seismic demand, even though it is part of an effective stress phenomenon; and (3) because it is based on a database of observed surface manifestations, there are uncertainties when it is applied outside of database (e.g., depths > 10 m).

Figure 2 shows the possible combinations from which the safety factor against liquefaction can be determined. Indeed, both CSR and CRR can be defined by using two possible levels of accuracy:

- Level *A* or *a*, respectively, for CSR and CRR: where the minimum effort is requested in terms of both experimentation and calculation to define FS. This is the most immediate and largely adopted level in codes and guidelines;
- Level *B* or *b*, respectively, for CSR and CRR: where a bigger effort is required compared to level *A/a* to define FS in terms of both experimentation and calculation.

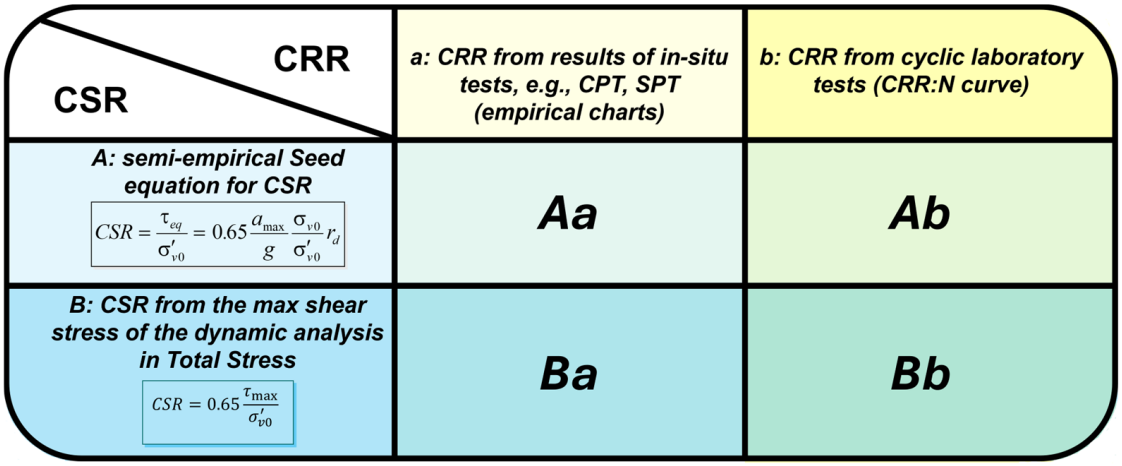


Figure 2. Calculation of the safety factor according to different analysis levels.

In detail, from the perspective of the seismic demand, the CSR can be calculated as follows:

- Level *A*: hand-made calculation according to the simplified expression:

$$\mathrm{CSR} = 0.65 \frac{\tau_{max}}{\sigma\prime_v} = 0.65 \cdot \frac{a_{max}}{g} \cdot \frac{\sigma_v}{\sigma\prime_v} \cdot r_d \quad (10)$$

where σ_v is the total vertical stress and σ'_v is the vertical effective stress at a depth z, a_{max} is the maximum horizontal acceleration expected at the ground surface, 0.65 is the coefficient introduced to have an equivalent constant shear stress amplitude starting from the maximum shear stress, τ_{max}, g is the gravity, and r_d is a reduction factor accounting for soil deformability, usually a function of the depth and moment magnitude, M_w, of the seismic event [68].

- Level *B*: the results of total stress ground response analysis, processed according to the equation:

$$CSR = 0.65 \frac{\tau_{max}}{\sigma'_v} \quad (11)$$

where τ_{max} is the maximum shear stress coming from the seismic site response analysis in total stress at the depth z, 0.65 is the coefficient adopted to convert the irregular loading into an equivalent constant shear stress amplitude, and σ'_v is the vertical effective stress.

The earthquake scenario is defined only by the pair made by the maximum expected acceleration at the site and the moment magnitude of the seismic event (a_{max}, M_w) at the basic level *A*, while a selection of accelerograms, typically spectro-compatible with a target spectrum [72], is required for level *B*. In addition, in level *B*, for performing the total stress ground response analysis, even in the most simple one-dimensional configuration, it is necessary to define the depth of the seismic bedrock, the stratigraphy of the soil layering, the soil properties of each deformable soil deposits in terms of unit weight, shear wave velocity, and non-linear and dissipative soil behavior (usually expressed as normalized shear modulus and damping ratio vs. shear strain curves). Therefore, in level *B*, the better accuracy in the definition of the CSR is because the τ_{max} is accounting for the seismic soil response to the applied shaking, while, in level *A*, the local site effects are only accounted in the definition of a_{max} via the amplification factors [72].

From the perspective of cyclic soil resistance, the CRR can be calculated as follows:

- Level *a*: empirical equations that correlate the CRR to the results of normalized mechanical soil parameters as obtained from in situ tests, e.g., Cone Penetration Test—CPT [68,70], Standard Penetration Test—SPT [68], Flat Dilatometer Test—DMT [73], and shear wave velocity measurement [74,75]. An example of an empirical relationship between CRR for the reference conditions (M_w = 7.5; σ'_{v0} = 1 atm) and the normalized corrected blow count, $(N_1)_{60cs}$, as measured during SPT, or the normalized and corrected cone tip resistance of CPT, q_{c1NCS}, is proposed by [68] as follows:

$$CRR_{M=7.5,\sigma'=1} = \exp\left(\frac{(N_1)_{60cs}}{14.1} + \left(\frac{(N_1)_{60cs}}{126}\right)^2 - \left(\frac{(N_1)_{60cs}}{23.6}\right)^3 + \left(\frac{(N_1)_{60cs}}{25.4}\right)^4 - 2.8\right) \quad (12)$$

$$CRR_{M=7.5,\sigma_v'=1} = \exp\left(\frac{q_{c1Ncs}}{113} + \left(\frac{q_{c1Ncs}}{1000}\right)^2 - \left(\frac{q_{c1Ncs}}{140}\right)^3 + \left(\frac{q_{c1Ncs}}{137}\right)^4 - 2.8\right) \quad (13)$$

- Level *b*: direct estimation of the cyclic soil resistance via the cyclic resistance curve, i.e., the relationship between the cyclic resistance ratio and the number of cycles necessary to induce liquefaction as measured by cyclic simple shear or cyclic triaxial tests. However, laboratory tests have some limitations to reproduce the site conditions and consequently some corrections need to be applied prior to using the curve for engineering applications [69,76–78].

Level *b* is characterized by higher accuracy compared to Level *a* due to the fact that the relationship between CRR and N is directly investigated for the considered soil. This implies that the estimation of the excess pore water pressure can be performed both following a direct way via the normalized number of cycles, as for Equation (1) or Equation (5), or an indirect way via the relationship between r_u and the safety factor, FS. Further insights are provided in the next subsections on *Ab* and *Bb* levels.

The FS calculation according to the method *Aa* is the most popular and adopted in several building codes and guidelines [72], while the method *Bb* is less popular due to the difficulty of having undisturbed samples of liquefiable soils to be properly tested in a laboratory. The hybrid combination *Ba* and *Ab*, even though characterized by a different level of accuracy, is still possible if a site is well-documented enough to allow the execution of a ground response analysis in total stress but cyclic laboratory tests are missing (method *Ba*) or if the cyclic resistance curve is experimentally available for the liquefiable layer but other data for seismic response analysis are not available (method *Ab*). This last case is quite rare in practical applications.

More insights into the four combinations are provided in the following subsections, with special focus on level *Aa* and *Bb*.

3.1. Level Aa: Safety Factor Calculated by Using the Semi-Empirical Equation for CSR and Empirical Charts for CRR

According to this level, the factor of safety is as follows:

$$FS = \frac{CRR}{CSR} = \left(\frac{CRR_{M=7.5,\sigma'_v=1}}{CSR}\right) \cdot MSF \cdot K_\sigma \cdot K_\alpha \quad (14)$$

where CSR is calculated according to Equation (10), $CRR_{M=7.5,\sigma'v=1}$ represents the cyclic resistance ratio (CRR) normalized to a seismic magnitude of M_w = 7.5 and to a reference effective overburden stress of σ'_v = 103 kPa, and Magnitude Scaling Factor (MSF) is incorporated to account for the influence of the earthquake duration. Finally, K_σ and K_α are correction factors accounting for the effects of the effective overburden stress and the initial static shear stress on the horizontal plane, respectively [67,68].

After the definition of FS, a rough estimation of the seismic-induced excess pore pressure ratio (r_u) can be performed using one of the relationships between r_u and FS, such as reported by Iwasaki et al. [79], Marcuson et al. [80], and Chiaradonna and Flora [81]. The latter proposed the following expression:

$$r_u = \frac{2}{\pi}\arcsin\left[FS^{-\frac{1}{2b\beta}}\right] \text{ for } FS > 1 \quad (15)$$

where the exponents b and β can be estimated as a function of normalized SPT blow count, $(N_1)_{60cs}$, or as a function of normalized and corrected cone tip resistance of CPT, q_{c1NCS}, and estimated fines content, FC. The analytical expressions for b and β are the following:

$$b = -1.487 \cdot 10^{-8} \cdot {q_{c1Ncs}}^3 + 1.291 \cdot 10^{-5} \cdot {q_{c1Ncs}}^2 - 5.722 \cdot 10^{-4} \cdot q_{c1Ncs} + 0.163 \quad (16)$$

$$b = -1.000 \cdot 10^{-6} \cdot \left({(N_1)_{60cs}}^3 + 2.216 \cdot 10^{-4} \cdot \left({(N_1)_{60cs}}^2 + 1.727 \cdot 10^{-3} \cdot (N_1)_{60cs} + 0.1557\right.\right. \quad (17)$$

$$\beta = 0.01166 \cdot FC + 0.3536 \cdot \left(q_{c1Ncs} - \Delta q_{c1N}\right)^{0.264} - 0.4979 \quad (18)$$

$$\beta = 0.01166 \cdot FC + 0.1091 \cdot \left((N_1)_{60cs} - \Delta(N_1)_{60}\right)^{0.5} + 0.5058 \quad (19)$$

where Δq_{c1N} and $\Delta(N_1)_{60}$ are the increment components of the normalized soil parameters, q_{c1NCS} and $(N_1)_{60cs}$, due to the beneficial effects of the fines content on the soil cyclic resistance for CPT and SPT, respectively [68].

Figure 3 shows the r_u-FS charts for different FC values.

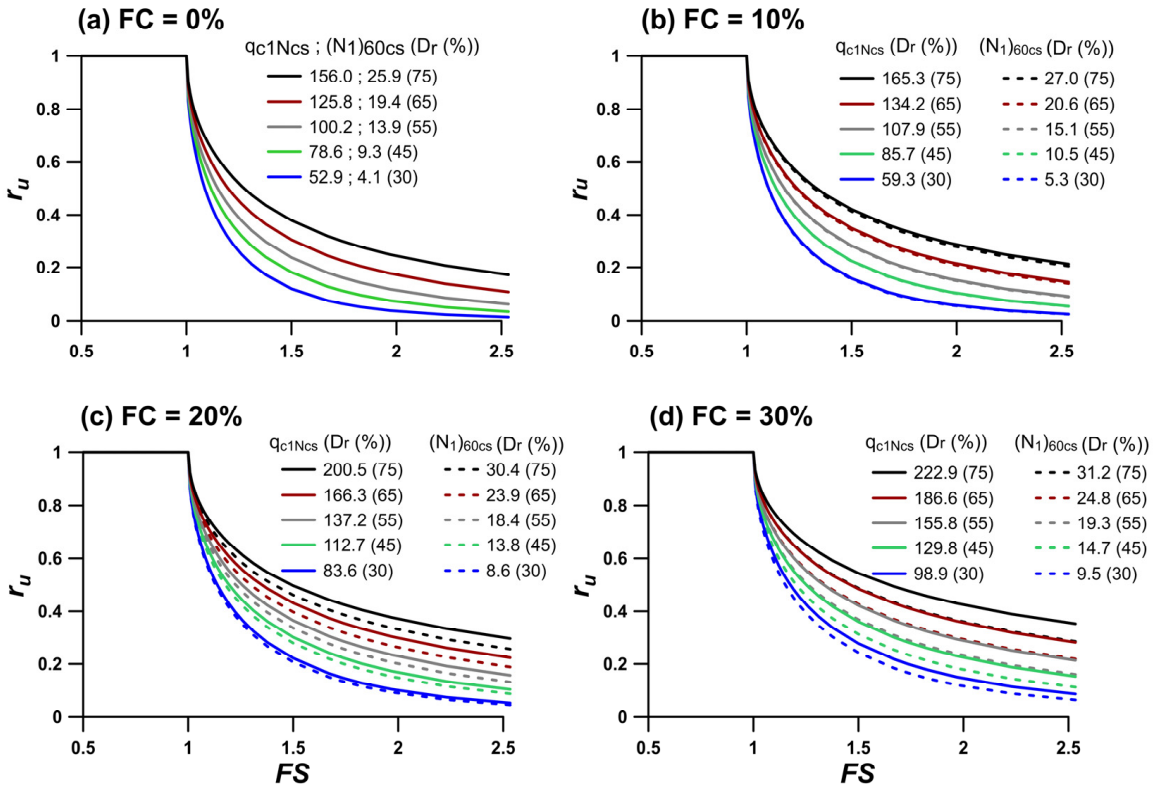


Figure 3. Charts r_u vs. FS for fines content equal to (**a**) 0%, (**b**) 10%, (**c**) 20%, and (**d**) 30% (modified after [81]).

Example Application for Level *Aa*

During the 30 October 2020 earthquake, water eruptions were observed at the basement level of a residential building equipped with stone columns in Izmir city center [82]. This residential structure is located 2.6 km inland (from the shoreline), where the groundwater table was detected 1 m below ground level. Foundation and subsoil data are constrained, having been sourced from the original geological–geotechnical investigation report prepared during the building's construction. To mitigate soil liquefaction potential, an array of 199 vertical drains was installed beneath the foundation. After the 2020 earthquake, a water eruption was observed from the vertical drains/columns, with water visible on the basement floor. The absence of finishes in this embedded story allowed for clear visibility of the effusive event. Eyewitness accounts confirm that the floor remained saturated for several days post-event. No external liquefaction manifestations (e.g., sand boils) or ground bulging was observed around the structure or in the vicinity.

Representative soil column consists primarily of sandy soils with variable content of silty or clay fines in the first 10 m below the ground level. Quantitative data on soil properties were derived from SPT performed at four locations beneath the building's corners, with a mean SPT N-value of 10 observed within the upper 10 m (Figure 4).

According to level *Aa*, a two-step procedure was implemented for the analysis of soil response under seismic loading: the initial step involved estimating the liquefaction potential of the underlying soil layers. This was achieved by calculating FS using the SPT chart according to [68]; the second step focused on a preliminary evaluation of r_u through Equation (15). The expected r_u ranges in the interval 0.1–0.4, with a maximum of 0.8 at 7 m (Figure 4). A hydraulic gradient of 3–6 m of the water column is associated to this result, which is enough to activate the vertical drains.

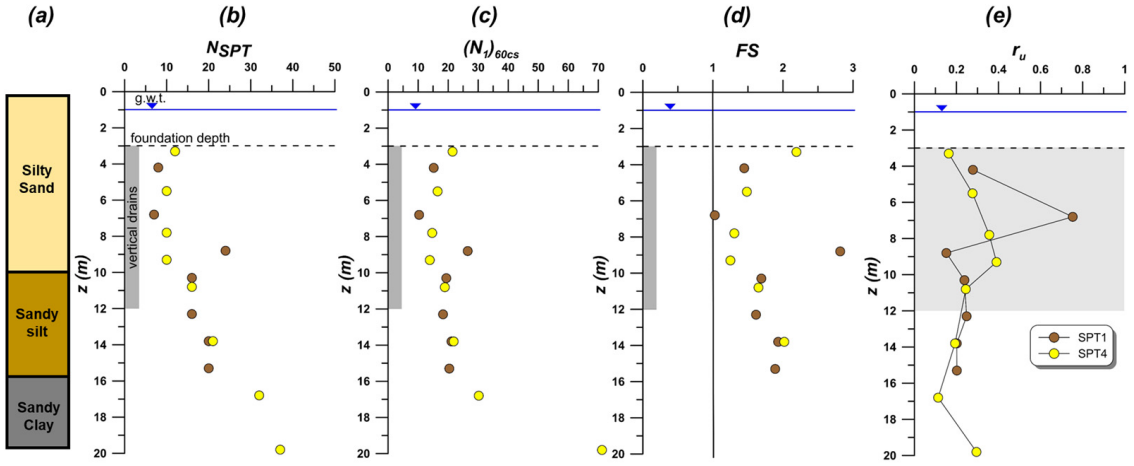


Figure 4. Izmir case study: Soil column with vertical profiles of (**a**) measured and (**b**) corrected and normalized SPT blow count (**c**), factor of safety (**d**), and pore pressure ratio (**e**). Modified after [82].

3.2. Level Ba: Safety Factor Calculated by Using Dynamic Total Stress Analysis for CSR and Empirical Charts for CRR

The estimation of r_u for level *Ba* follows the same procedure of level *Aa*, i.e., a two-step procedure made up of an FS calculation via Equation (14) and a r_u calculation via Equation (15). The only difference between level *Ba* and *Aa* is the fact that CSR comes from a seismic site response analysis in total stress via Equation (11), and not from the application of Equation (10).

3.3. Level Bb: Safety Factor Calculated by Using Dynamic Total Stress Analysis for CSR and Cyclic Resistance Curve for CRR

The estimation of r_u for level *Bb* follows a three-step procedure consisting of the following: (1) performing a total stress ground response analysis; (2) defining for each depth of the liquefiable layer the pair (CSR, N_{eq}), where CSR is calculated according to Equation (11) and N_{eq} is calculated with one of the available relationships for estimating an equivalent number of cycles, e.g., Biondi et al. [38]; (3) estimating r_u in a direct way (*d* in Figure 1) as a function of the normalized number of cycles, e.g., by applying Equation (1) or Equation (5), or in an indirect way (*i* in Figure 1) as a function of the safety factor, e.g., by applying Equation (15).

Figure 5 shows a scheme with the three steps described above.

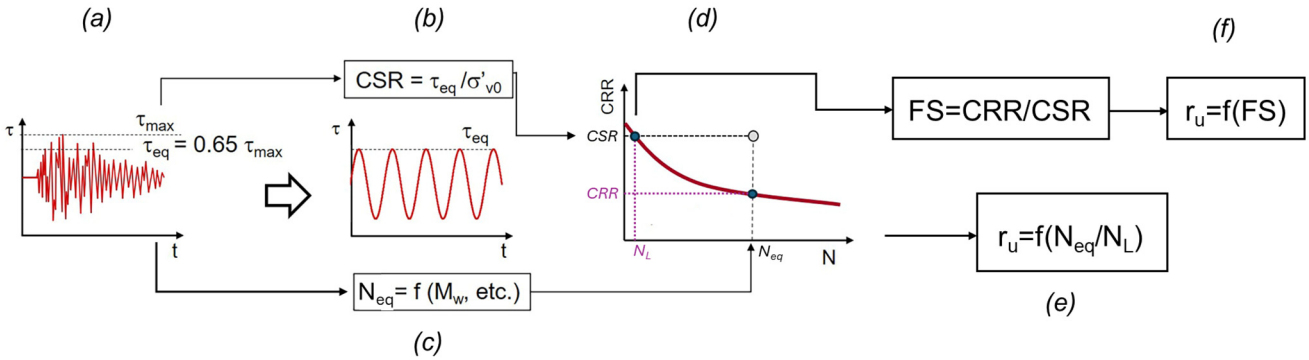


Figure 5. Estimation of r_u for the *Bb* level: (**a**) total stress dynamic analysis, (**b**) definition of CSR via Equation (11) and (**c**) definition of the equivalent number of cycles for the considered earthquake to convert the irregular time history into a regular history of N_{eq} cycles with CSR amplitude, (**d**) comparison of the pair (CSR, N_{eq}) with the cyclic resistance curve, calculation of r_u as a function of (**e**) N_{eq}/N_L (direct way) or (**f**) FS = CRR/CSR (indirect way). Modified after [83].

3.4. Level Ab: Safety Factor Calculated via the Semi-Empirical Equation for CSR and the Cyclic Resistance Curve for CRR

The estimation of r_u for level *Ab* follows a two-step procedure consisting of the following: (1) defining for each depth of the liquefiable layer the pair (CSR, N_{eq}), where CSR is calculated according to Equation (10) and N_{eq} is calculated with one of the available relationships for estimating an equivalent number of cycles, e.g., Biondi et al. [38]; (2) estimating r_u in a direct way (*d* in Figure 1) as a function of the normalized number of cycles, e.g., by applying Equation (1) or Equation (5), or in an indirect way (*i* in Figure 1) as a function of the safety factor, e.g., by applying Equation (15).

4. Simplified Methods

Simplified methods can be considered an upgrade of the *B*-level methods as described in the previous sections, where the time history of a reference variable (e.g., shear strain, shear stress or dissipated energy) is extracted from the results of the seismic site response analysis in total stress and is processed in a pore pressure generation model according to a decoupled approach. In the stress-based approach, instead of considering the maximum shear stress only as for the *B*-level of synthetic methods, the entire time history of the shear stress is processed in a stress-based pore pressure model, such as the PWP model based on the damage parameter described above. An exemplificative application is reported for a real case study in the following Section 7.2. A further application for an ideal soil column is reported in Appendix A.1.

5. Approximate Methods

The approximate methods include all the codes for seismic response analysis in effective stress, where a loosely coupled approach is adopted. This level of analysis enables the incorporation of the dissipation of the generated excess water pressure into the calculations depending on the hydraulic boundary conditions. This is not possible in the decoupled approach. In the following Section 7.3, an example is provided for the simplified PWP model based on the damage parameter, which is implemented in the one-dimensional code SCOSSA [84]. A further example for an ideal soil column is reported in Appendix A.2 This latter aims to highlight the difference between the decoupled (simplified) and coupled (approximate) analysis.

6. Rigorous Methods

The rigorous methods include all the effective stress ground response analysis, where a fully coupled approach is adopted. An application is reported for a real case study in the following Section 7.4. A further example aiming to show a comparison between the approximate and the rigorous method is reported in Appendix A.3.

7. Application of Hierarchical Methods to a Case Study

The described methods are applied in this section to a liquefaction case study: a site in Pieve di Cento (Bologna province) located in an area that experienced liquefaction manifestations after the 2012 Emilia Earthquake [85] and was the setting of a real-scale liquefaction experiment in October 2018 [86,87].

Chiaradonna et al. [88] numerically investigate the dynamic response of the site for several seismic scenarios with a return period, T_R, ranging from 50 to 2475 years, associated with a probability of exceedance, P_{VR} in 50 years [72], ranging between 63% and 2%. For the proposed study, the earthquake scenario with a T_R = 140 years (P_{VR} = 50%) is considered, which is the most severe among those analyzed in [88] that do not induce the full liquefaction of the liquefiable deposits. For the sake of simplicity and making

the logical flow more understandable, only one of the seven selected acceleration records will be considered in the following, i.e., the East–West component of the M_w = 5.2 12 October 1997 Central Italy earthquake recorded at the FORC recording station [89]. Figure 6 reports the time history of acceleration used in dynamic analyses. Further details about the definition of the input motion adopted in the analyses can be found in Chiaradonna et al. [88] and are omitted here for the sake of brevity.

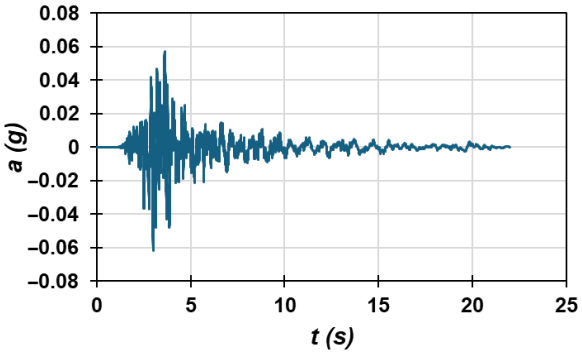


Figure 6. Reference input motion used in the dynamic analyses.

An extensive in situ campaign [86] provided the data for soil characterization. The stratigraphy is composed of several distinct units (Figure 7a), beginning with a 0.9 m thick surficial crust of silty sand (SS1), which transitions into a sandy silt layer extending to approximately 2.9 m depth, partially above (SS2) and below (SS3) the groundwater table, which is located at 1.8 m depth. Below this, a grey silty sand layer (GSS) is encountered between 2.9 m and 6.0 m, interrupted by a thin intermediate clayey layer (Clay1) situated between 4.4 m and 4.8 m. From the 6.0 m mark to the maximum investigated depth, a thick silty clayey deposit (Clay2) dominates the profile. The upper sandy silty layer (SS) is characterized by heterogeneity (well-graded, with low-plasticity fine content ranging from 60% to 85%), whereas the deeper GSS is more homogeneous, exhibiting a narrow fine content range of 5% to 12% (Figure 8b). The clay deposit has a plasticity index, PI, equal to 0.55 and a percentage of clay ranging from 50 to 80%. The Soil Behavior Type index [90] resulting from in-situ tests is illustrated in Figure 8a. Based on susceptibility analyses, the GSS deposit has been identified as the liquefiable critical layer (Figures 7e and 8a). This finding is supported by a combination of factors, including full saturation, loose state (Dr = 40%), low effective stress state, and an average SBT < 2.0 (Figure 8a).

7.1. Synthetic Methods Application

According to level *Aa*, soil capacity (CRR) was estimated on CPT-based chart reported by [68], while the seismic demand (CSR) was calculated by Equation (10) where a_{max} was equal to the stratigraphic amplification factor multiplying the maximum expected acceleration value on rock formation defined for a T_R = 140 years and the mean magnitude defined from the de-aggregation map of the selected site as reported in the Italian seismic hazard model [91,92], i.e., PGA = 0.094; M_w = 4.93.

For the application of charts in Figure 3, it is of outmost importance to have a reliable estimation of the fines content of soils. For this case study, an estimate of the fines content has been carried out as a function of the SBT index according to the relationship proposed by [68]:

$$FC = 80(I_c + C_{FC}) - 137 \quad (20)$$

where the error coefficient C_{FC} has been calibrated specifically for this site on the basis of the grain size distribution curves and I_c profiles (Figure 8), and it is equal to −0.0775.

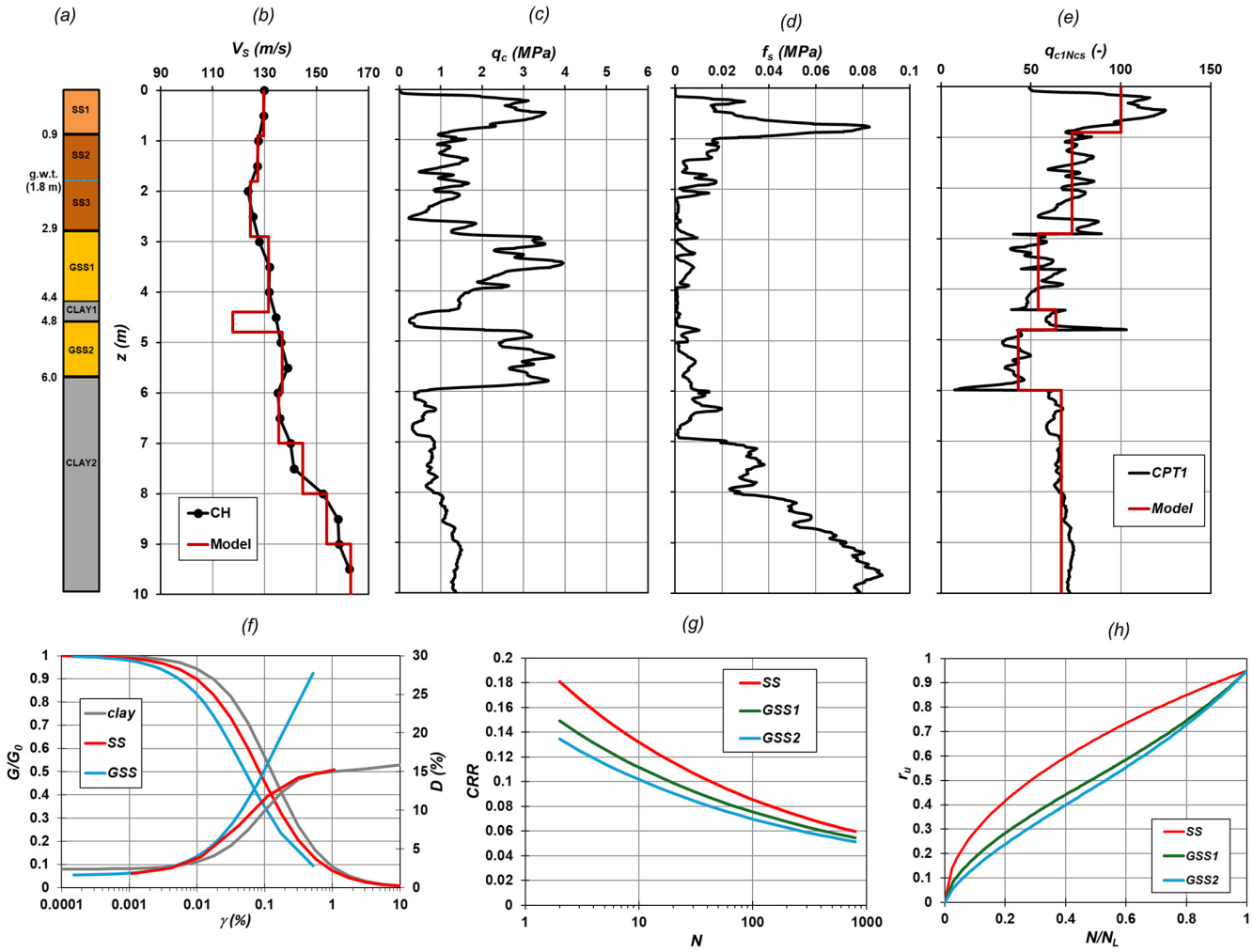


Figure 7. (**a**) Reference soil column; profiles of (**b**) shear wave velocity (in red profile used in the model), (**c**) cone tip resistance, (**d**) sleeve friction resistance, and (**e**) normalized and corrected cone tip resistance (in red profile used in the model), (**f**) normalized shear modulus and damping ratio vs. shear strain, (**g**) cyclic resistance curves, and (**h**) pore pressure ratio vs. normalized number of cycles used in the PWP model (modified after [88]).

The excess pore pressure ratio profile for level *Aa* is reported in Figure 9g. Liquefaction is attained in the GSS2 layer, while it is only locally attained in the above GSS deposit.

According to level *Ba*, seismic site response analysis in total stress has been performed with the code STRATA [90] for the estimation of the seismic demand (CSR), while soil capacity (CRR) was quantified on the empirical chart proposed by [68], as in the previous level.

For the execution of the dynamic analysis in total stress, it was necessary to define the geotechnical model of the site, i.e., the shear wave velocity profile and the shear modulus reduction curves, and damping ratio curves vs. shear strain for each soil unit. The shear wave velocity profile was established based on the results obtained from a Cross-Hole (CH) test conducted in situ [86]. Figure 7b shows the experimental profile of the shear wave and the one adopted in the model. The investigation into the non-linear and dissipative characteristics of the soils was obtained by conducting cyclic torsional shear tests specifically on the grey silty sand (GSS) deposits (Figure 7f). For the remaining soil layers (Figure 7f), namely the silty sand (SS) and clay formations, the constitutive behavior was characterized by utilizing experimental curves derived from tests performed on Scortichino deposits,

which are located approximately 20 km away. This approach was adopted due to the substantial geological similarity between the Scortichino and Pieve di Cento sites [93,94].

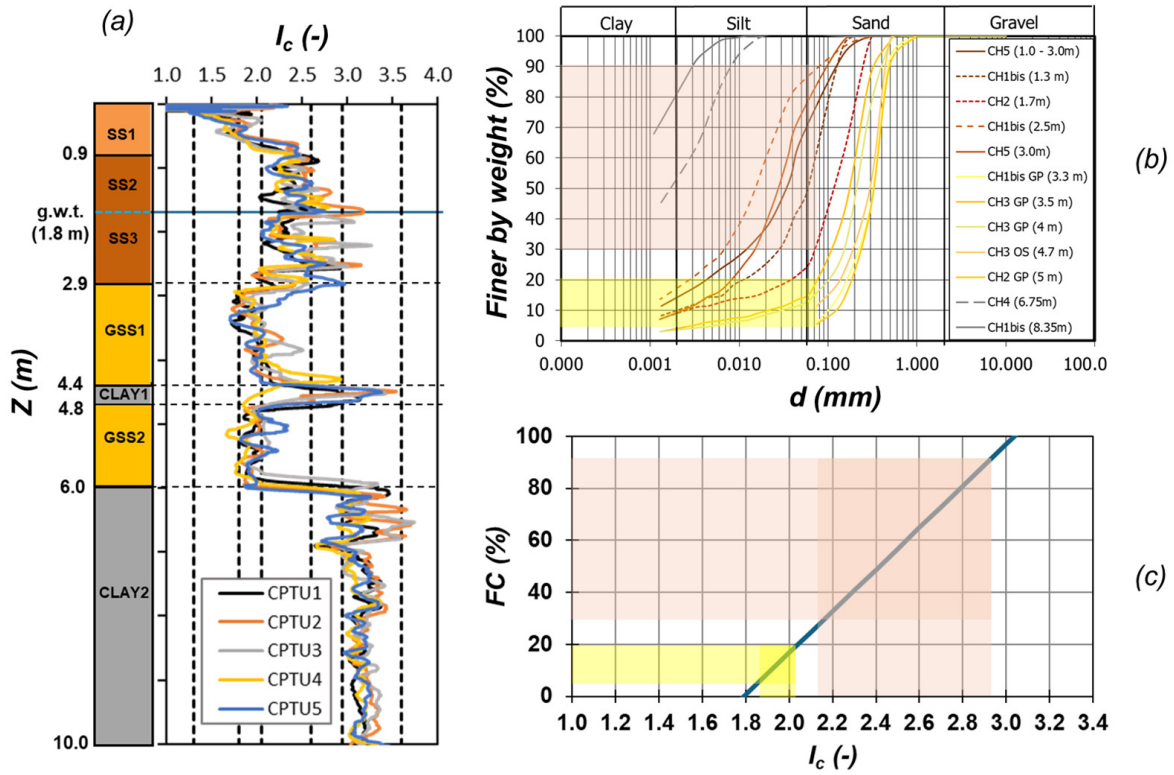


Figure 8. (**a**) Soil stratigraphy with the vertical profiles of the SBT index as obtained from CPTUs; (**b**) grain size distribution curves of the three main units; (**c**) calibrated relationship between FC and I_c proposed by [68].

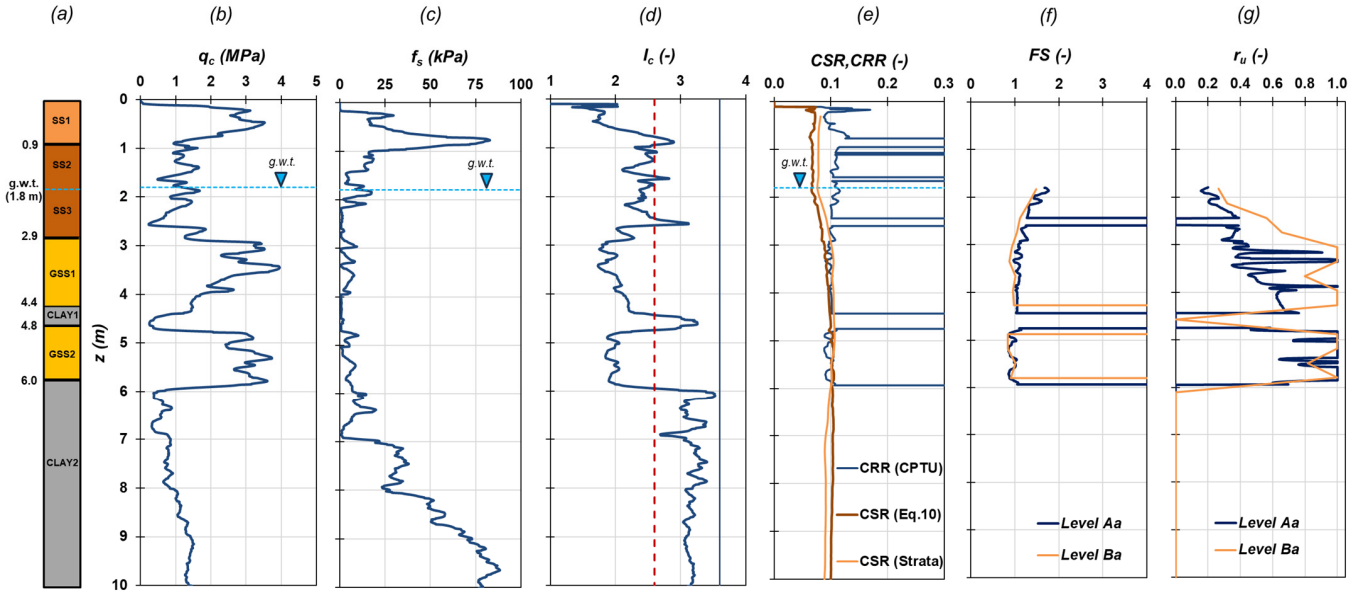


Figure 9. (**a**) Soil stratigraphy, (**b**) cone tip resistance, (**c**) lateral resistance, (**d**) Soil Behavior Type index, (**e**) cyclic resistance and cyclic stress ratios, (**f**) safety factor, (**g**) excess pore water pressure ratio from *Aa* and *Ba* levels of analysis.

Figure 9 compares the obtained pore water pressure ratio profile for the *Ba* level with that from the *Aa* level. The seismic demand defined from the dynamic analysis is slightly

higher than the CSR from Equation (10) at the depth of the liquefiable layers (Figure 9e), implying a slightly lower FS to which is associated with a higher r_u profile.

According to level *Ab*, the seismic demand, CSR, is the same as the previous *Aa* level based on Equation (10), while the cyclic strength of soils is directly defined by the cyclic resistance curves of the three liquefiable units (Figure 7g). In this case, the cyclic resistance curve is required to define an equivalent number of cycles for the considered motion. Due to the simplicity of the CSR definition, the relationship proposed by Idriss [95], which is only a function of magnitude, was adopted. For a magnitude of approximately 5, the Idriss [95] relationship leads to an equivalent number of cycles of 2 (Figure 10). In this case, the number of cycles is independent of the depth (Figure 11a). The pair at each depth (N_{eq}, CSR) is used to examine the cyclic resistance curve of each soil unit and define CRR and N_L, i.e., the soil resistance in correspondence with N_{eq} and the number of cycles to induce liquefaction for a CSR loading, respectively (Figure 10). The ratio N_{eq}/N_L is used to estimate the r_u via Equation (5), calibrated as reported in Figure 7h according to the direct way (Figure 11d—continuous black line). Alternatively, according to the indirect way, the FS is first calculated as CRR/CSR (Figure 10) and then the r_u calculated according to Equation (15), where the coefficients b and β are estimates as a function of the CPTU results (Equations (16) and (18), respectively). The vertical profiles of r_u are reported in Figure 11d. The variability between the direct and indirect ways is quite limited.

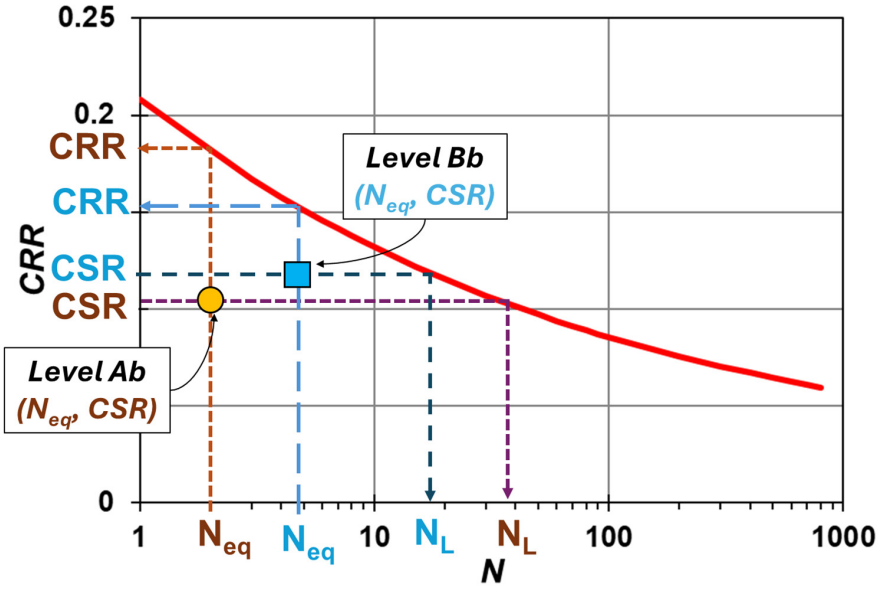


Figure 10. Estimation of r_u for the *Ab* level (brown lines and labels) and *Bb* level (blue lines and lables) at the 2.74 m depth: seismic demand expressed in terms of N_{eq} and CSR compared with the cyclic resistance curve. Identified parameters CRR, N_L, are then used for the calculation of r_u as a function of Neq/N_L (direct way) or FS = CRR/CSR (indirect way).

According to level *Bb*, the seismic demand was estimated from the total stress analysis in terms of maximum shear stress (Equation (11)), while the cyclic strength of soils is directly defined by the cyclic resistance curves of the three liquefiable units (Figure 7g). With respect to the previous case, at each depth a time history of acceleration derived from dynamic analysis is available. As a consequence, it was possible to apply a more refined relationship for the quantification of the equivalent number of cycles, such as that proposed by Biondi et al. [38], where N_{eq} is a function of the PGA and Arias intensity of the accelerogram. The vertical profiles of N_{eq} are reported in Figure 11a. It is slightly higher than that adopted in the *Ab* level (see also Figure 10 for a specific depth). Consequently, this implies that the CRR is lower (Figure 10) as well as the FS, resulting in remarkably higher

r_u profiles in both direct and indirect ways (Figure 11d). The *b* level for the definition of the CRR, although characterized by better accuracy in the definition of the soil cyclic resistance, is affected by a large variability in the results due to the uncertainties connected to the definition of the equivalent number of cycles.

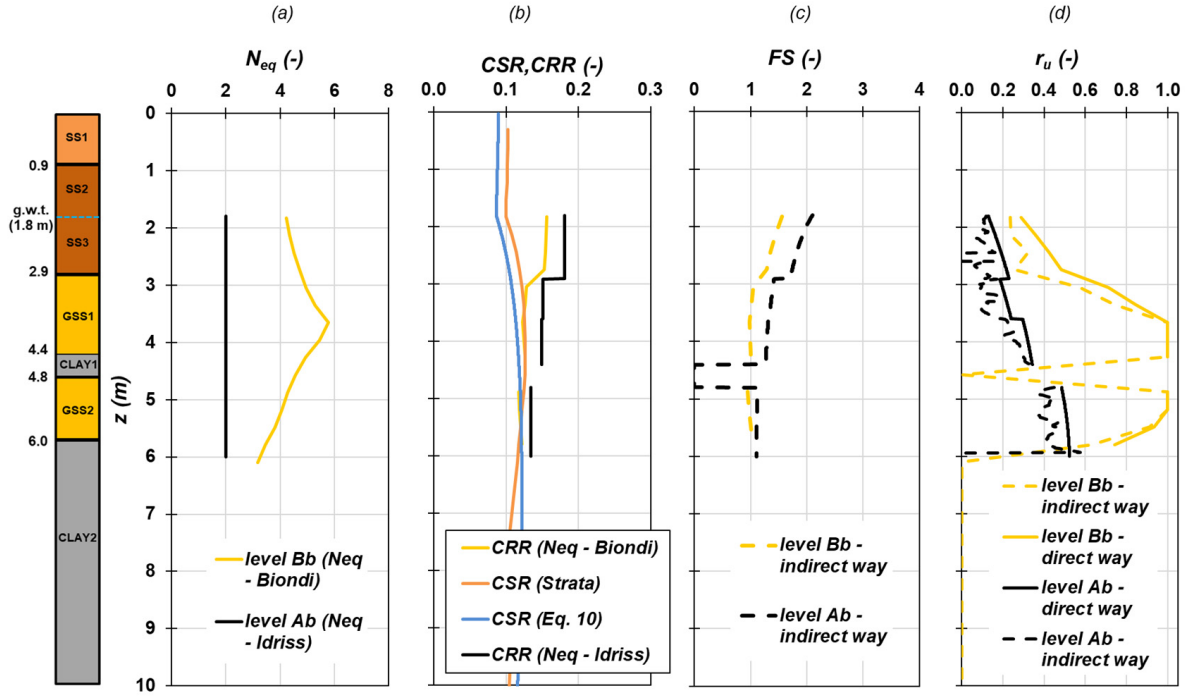


Figure 11. Vertical profiles of the (**a**) equivalent number of cycles, (**b**) cyclic resistance and cyclic stress ratios, (**c**) safety factors for indirect ways, and (**d**) excess pore water pressure ratio from *Ab* and *Bb* levels for direct and indirect ways.

7.2. Simplified Method Application

The simplified method described in Section 4 can be considered as an upgraded version of the *Bb* level, because the input data are substantially the same: the total stress dynamic analysis for the seismic demand and the cyclic resistance curve for the soil resistance. However, the conversion process to a uniform loading of the irregular shaking is bypassed thanks to the application of the PWP model, according to a decoupled approach. The PWP model, which requires determination of the cyclic resistance and excess pore water pressure curves (Figure 7g,h), was calibrated on the results of CPTU for GSS layers, according to [47]. Because the fines content exceeds 30%, the r_u-N/N_L relationship defined in the laboratory on Scortichino sandy silt [94] was adopted for the SS unit due to the similarity in the grain size distribution.

The histories of shear stress from the total stress analysis at all the available depths were processed with the PWP model to predict the time histories or r_u. Figure 12 shows the PWP model application at a representative depth of 2.7 m.

The damage parameter accumulates only when the normalized stress, τ^*, overcomes the threshold, CSR_t (dashed black line in Figure 12b).

Equation (2) is used to predict the excess pore pressure (Figure 12c,d). Higher values of r_u are attained in the first 10 s, where the intensity of the loading is the highest.

For each time history along the vertical depth gained from the total stress analysis, the process described in the above Figure 12 was applied. The resulting r_u profile is shown in Figure 13a,b (labeled as STRATA + PWP).

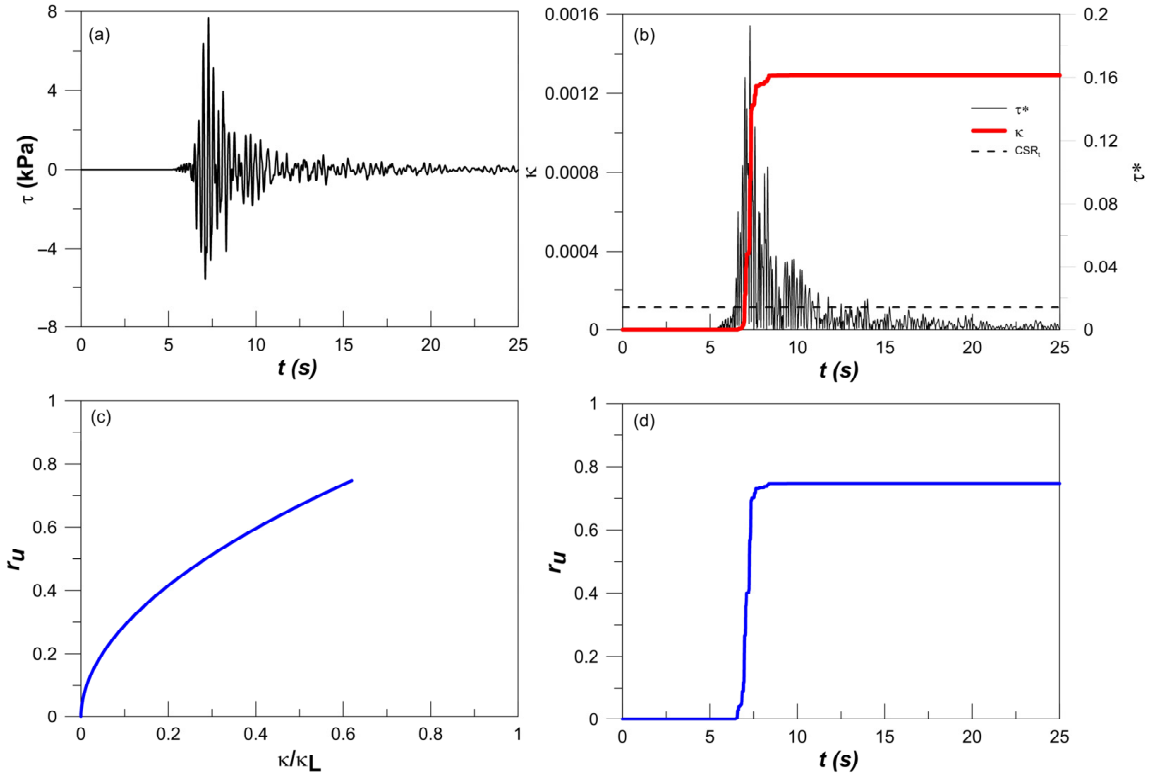


Figure 12. Decoupled analysis: (**a**) time history of shear stress at 2.7 m from the total stress analysis; (**b**) shear stress ratio and damage parameter accumulation vs. time; (**c**) excess pore pressure ratio vs. the normalized damage parameter; (**d**) predicted excess pore pressure ratio.

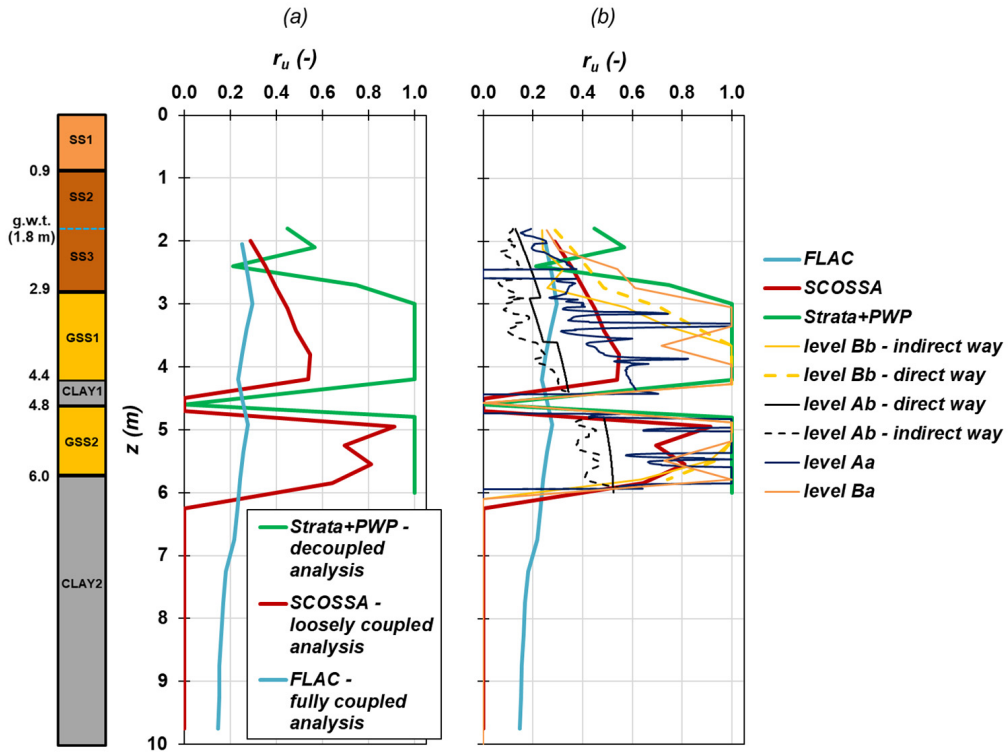


Figure 13. Vertical profiles of (**a**) the maximum excess pore pressure ratio from the time histories of the dynamic analyses, and (**b**) comparison of excess pore water pressure ratio profiles across different levels of analysis, ordered in the legend by decreasing complexity.

7.3. Approximate Method Application

Loosely coupled effective stress analysis in a one-dimensional condition has been performed with the code SCOSSA [44].

The only additional parameter that is new compared to the simplified method is the degradation parameter of the Matasovic and Vucetic [62] degradation model, which was set to the average of 3.5, consistent with the author's suggestions.

The remaining data for the analysis are the same used in the total stress analysis reported in Figure 7. The resulting r_u profile is shown in Figure 13a,b (labeled as SCOSSA).

7.4. Rigorous Methods Application

A fully coupled effective stress non-linear dynamic analysis has been carried out with the Finite Difference Method bidimensional code FLAC [96].

The liquefiable units (SS, GSS type) were modeled using the constitutive model PM4Sand version 3.1 [97], with the model parameters listed in Table 1.

Table 1. Calibrated parameters for PM4Sand and PM4Silt.

Parameter	SS1	SS2	SS3	GSS1	Clay1	GSS2	Clay2
Apparent relative density D_R	0.38	0.38	0.38	0.35	-	0.35	-
Undrained shear strength su/σ'_{v0}	-	-	-	-	0.25	-	0.25
Shear modulus coefficient, Go	1769	1021	791	548	511	534	473
Contraction rate parameter, h_{po}	0.7	0.7	0.7	0.82	26	0.85	27

Calibrations were developed for representative mean values of q_{c1Ncs}, with values of 66 and 60 for SS and GSS layers, respectively.

The shear modulus coefficient (Go) was calibrated on the in situ shear wave velocity, Vs, at the middle of the stratum, the apparent relative density (D_R) was estimated as 38% and 35% for SS and GSS layers, and the contraction rate parameter (h_{po}) was iteratively set to match the cyclic strength in 15 uniform cycles as predicted by the cyclic resistance curves of Figure 7g. All the secondary parameters were set to their default values.

The clay deposits were modeled using the constitutive model PM4Silt [98] with the parameters listed in Table 1. The Go was defined on the measurement of Vs at the middle of the layer. The h_{po} was adjusted to produce reasonable slopes for the cyclic strength curves of clay soils (obtained from CPTU), as reported by [69]. All the secondary parameters were set to their default values.

The resulting r_u profile is shown in Figure 13a,b (labeled as FLAC).

Figure 13a compares the r_u profiles obtained from the time histories of the three dynamic analyses. It is possible to observe that by increasing the level of complexity of the methods (simplified to approximate to rigorous level), the degree of conservatism of the analysis significantly decreases. This means that a major effort in the definition of the geotechnical model and complexity of the constitutive model, and also in the computational effort, is translated into benefits in cost saving and efficiency of the design process.

Figure 13b shows the comparison of the previous profiles with the synthetic methods. In this last case, there is no clear tendency but a large variability of the four levels. However, the basic *Aa* level is undoubtedly characterized by a great level of robustness compared to the other synthetic levels, due to the fact that it is based on the traditional safety factor calculation which is widespread throughout the world.

8. Utility of the Excess Pore Water Pressure Predictions

In addition to the identification of the liquefaction triggering (by definition), excess pore water pressure prediction can be used to verify the safety and serviceability of struc-

tures even in conditions far from failure or to correctly reproduce the system soil response recognized as the discriminating factor in observed or not-observed damage after strong earthquake sequences, just to mention two prominent problems.

In detail, the predicted excess pore water pressure can be used to contribute to the assessment of the following problems, although it is not limited to just these:

- Quantify the severity of sand ejecta manifestations [99–101];
- Estimation of the free-field consolidation settlements [102];
- Degraded bearing capacity of shallow foundations [103];
- Practical design of liquefaction mitigation interventions [104,105];
- Evaluating the influence of excess pore water pressure on permanent slope displacement during seismic action [106];
- Assessment of the uplift response of underground structures [107];
- Mapping vulnerability indexes of the liquefaction potential [108].

9. Discussion and Conclusions

This review aimed to provide a systematic classification of the existing methods for predicting excess pore water pressure induced by seismic loading.

Table 2 summarizes the required input data and the computational effort (i.e., the required resources) for each method of the hierarchy to guide a cost–benefit analysis for the choice of the most appropriate level.

Table 2. Summary of input data and the required effort of the hierarchical methods.

Method		Type of Computation	Type of Dynamic Analysis	Data for Seismic Demand	Data for Cyclic Soil Resistance	Calibration Effort	Computational Effort
Synthetic	Level *Aa*	Analytic	-	Max acceleration, magnitude	In situ test	-	Very low
	Level *Ab*	Analytic	-	Max acceleration, magnitude	Cyclic Resistance Curve	-	Very low
	Level *Ba*	Numerical	Total stress	Time history of the input motion	In situ tests	-	Low/ Medium
	Level *Bb*	Numerical	Total stress	Time history of the input motion	Cyclic Resistance curve	-	Low/ Medium
Simplified		Numerical	Total stress	Time history of the input motion	PWP model	Low	Low/ Medium
Approximate		Numerical	Loosely coupled effective stress	Time history of the input motion	Cyclic response + PWP model	Low/ Medium	Low/ Medium
Rigorous		Numerical	Fully coupled effective stress	Time history of the input motion	Advanced soil constitutive model	High	High

The basic level for estimating r_u from the safety factor against liquefaction (method *Aa*) is still not very common in engineering practice and should become much more popular in the future, in accordance with the performance-based design of structure and infrastructure.

The decoupled approaches provide conservative estimation of the pore water pressure compared to the coupled ones; however, their practical use is not always justified or convenient, especially for the simplified methods, because the same efforts of resources can easily lead to an approximate level.

The most accurate method we have at the moment is the rigorous one, which implies the use of advanced effective stress constitutive models; these are currently more accessible than in the past, thanks to guided calibration procedures provided by researchers [109,110].

The stress-based PWP model proposed by [45] can be applied transversally to all the different levels of complexity, and therefore, it seems a promising tool for predicting seismic-induced pore water pressure build-up in professional practice.

Future paths for the research can explore the applicability of hierarchical methods to several case studies with different seismic intensities to explore the range of variability of the results. It is worth mentioning that the findings of the present study should be further consolidated by analyzing a larger dataset of sites and seismic scenarios. This type of work has particular relevance for medium/low seismicity areas where remarkable excess pore pressure is expected more than complete liquefaction [111].

Supplementary Materials: The following supporting information can be downloaded at https://www.mdpi.com/article/10.3390/geosciences16020061/s1: Synthetic_LevelAa_LevelBa.xlsx.

Funding: Financial support was provided by the National Recovery and Resilience Plan (NRRP), Mission 4, Component 2, Investment 1.1, Call for tender No. 1409 published on 14 September 2022 by the Italian Ministry of University and Research (MUR), funded by the European Union—NextGenerationEU—Project Title "RI-SCOSSA 2.0—Renovation and Improvement of Seismic COde for Stick-Slip Analyses"—CUP P20228HN9M Grant Assignment Decree No. 1385, adopted on 1 September 2023 by the Italian Ministry of Ministry of University and Research (MUR).

Data Availability Statement: The data presented are available on request from the author.

Acknowledgments: The author would express gratitude to Antonio Gens and Marcos Arroyo from the Universitat Politecnica de Catalunya (UPC) for providing questions of great acumen that pushed the author to write the following review. The author would like to express her sincere gratitude to Ross W. Boulanger (University of California, Davis) for his invaluable guidance regarding the use of FLAC and the calibration of the PM4Sand and PM4Silt models. The author gratefully acknowledges the insightful feedback provided by the anonymous reviewers; their constructive comments and suggestions have significantly strengthened this review.

Conflicts of Interest: The author declares no conflicts of interest.

Abbreviations

The following abbreviations are used in this manuscript:

PWP	Pore Water Pressure
CSR	Cyclic Stress Ratio
CRR	Cyclic Resistance Ratio
PGA	Peak Ground Acceleration
FS	Factor of Safety
SPT	Standard Penetration Test
CPTU	Cone Penetration Test with pore water pressure measurement
CPT	Cone Penetration Test
SBT	Soil Behavior Type
PI	Plasticity Index
MSF	Magnitude Scaling Factor
FC	Fines Content
GSS	Grey Silty Sand
SS	Silty Sand
CH	Cross-Hole test
NS	North–South

Symbol	Unit	Description
r_u	-	Excess pore pressure ratio
σ'_{v0}	kPa	Initial effective vertical stress
σ'_v	kPa	Effective vertical stress
σ_v	kPa	Total vertical stress
Δu	kPa	Excess pore pressure
CSR_t	-	Horizontal asymptote of Equation (4)
CSR_r	-	Reference point of Equation (4)
α	-	Exponent of Equation (4)
a	-	First coefficient of Equation (2)
b	-	First exponent of Equation (2)
c	-	Second coefficient of Equation (2)
d	-	Second exponent of Equation (2)
q_{c1Ncs}	-	Normalized and corrected cone tip resistance
$(N_1)_{60cs}$	-	Normalized and corrected number of blow count
Δq_{c1N}	-	CPT cone tip resistance increment due the FC
$\Delta(N_1)_{60}$	-	SPT blow count increment due to FC
Dr	%	Relative density
PI	-	Plasticity index
a_{max}	g	Maximum acceleration
z	m	Depth
$K\sigma$	-	Overburden stress correction factor of Equation (14)
$K\alpha$	-	Initial static shear stress correction factor of Equation (14)
P_{VR}	%	Probability of exceedance in the reference period V_R
T_R	years	Return period
M_w	-	Moment Magnitude
V_S	m/s	Shear wave velocity
ρ	Kg/m^3	Soil density
γ	%	Shear strain
G/G_0	-	Shear modulus normalized to the initial value
D	%	Damping ratio
N	-	Number of cycles
D_R	-	Apparent relative density of PM4Sand model
G_o	-	Shear modulus coefficient of PM4Sand/Silt model
h_{po}	-	Contraction rate parameter of PM4Sand/Silt model
su/σ'_v	-	PM4Silt parameter
τ	kPa	Shear stress
τ_{max}	kPa	Maximum shear stress
τ^*	-	Normalized shear stress
N_L	-	Number of cycles causing liquefaction
N_{eq}	-	Equivalent number of cycles
r_d	-	Depth reduction factor of Equation (10)
β	-	Exponent of Equations (1) and (15)
b	-	Exponent of Equation (15)
C_{FC}	-	Correction factor of Equation (20)

Appendix A

Appendix A.1. Example Application for Simplified Method

An ideal soil profile is a 30 m-thick silty sand layer, with the groundwater table being 1 m in depth from the ground level (Figure A1a).

The input motion applied at the base of the soil column is the North–South (NS) component of the Umbria–Marche seismic sequence main shock (26 September 1997, $M_w = 6$), specifically the acceleration time history available at the Assisi recording station

(ASS), which exhibited a PGA of 0.273 g (Figure A1b). This record was applied as an outcrop motion at the bedrock, which was modeled as a viscoelastic half-space. The shear wave velocity profile was defined by a power function of depth with an exponent of 0.25, yielding a surface V_S of 100 m/s (Figure A1a). Soil non-linearity and dissipation were captured using experimental curves [112] derived from applying the cyclic response model (Figure A1c). The pore pressure model parameters (Equations (4) and (5)) were both calibrated against cyclic simple shear test data reported by Porcino and Diano [113].

A total stress dynamic analysis was performed, and then the shear stress history from the total stress analysis at 3 m depth was subsequently used with the pore pressure model to predict cyclic-induced pore pressure build-up time history, as shown in Figure A2.

The damage parameter accumulates only when the normalized stress overcomes the threshold parameter CSR_t (dot–dash black line in Figure A2b).

Equation (2) is used to predict the excess pore pressure (Figure A2c,d). Higher values of r_u are attained in the first 10 s, where the intensity of the loading is the highest (Figure A2a).

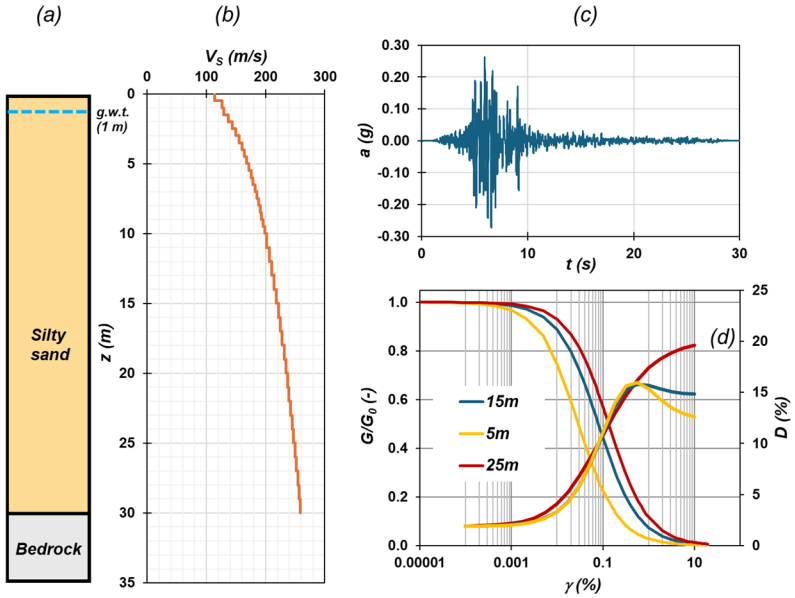


Figure A1. (**a**) Ideal soil column, (**b**) profile of shear wave velocity, (**c**) input motion, and (**d**) normalized shear modulus and damping ratio vs. shear strain (modified after [84]).

Appendix A.2. Example Application for Approximate Methods

Effective stress calculations employed a loosely coupled approach and a total stress calculation adopting a decoupled approach was compared in this section on the same ideal soil profile described in the previous Appendix A.1.

The input data for the analysis are those already described in the previous Appendix A.1. The only additional parameter that is new compared to the simplified method is the degradation parameter of the Matasovic and Vucetic [62] degradation model, which was set to the mean value of 3.5, consistent with the author's suggestions.

Results (Figure A3) demonstrate that the effective stress analysis computes lower maximum acceleration along the column's first 3 m and between 9 m and 19 m (Figure A3a) and mobilizes higher shear strains in the shallowest section due to stiffness degradation caused by excess pore pressure generation (Figure A3b). Coupled and decoupled maximum shear stress profiles show minor variations, though the decoupled analysis exhibits slightly higher stress amplitude because the maximum shear stress is less influenced by excess pore water pressure accumulation (Figure A3c). Consequently, the decoupled approach calculates higher pore water pressures than the coupled approach, resulting in liquefaction conditions within the shallowest 5 m of the soil column (Figure A3d). For comparison, the

vertical profiles obtained in a coupled analysis with partially drained conditions are also shown in Figure A3. The dissipation process seems to have a minor effect on the vertical profile of the maximum excess pore pressure ratio.

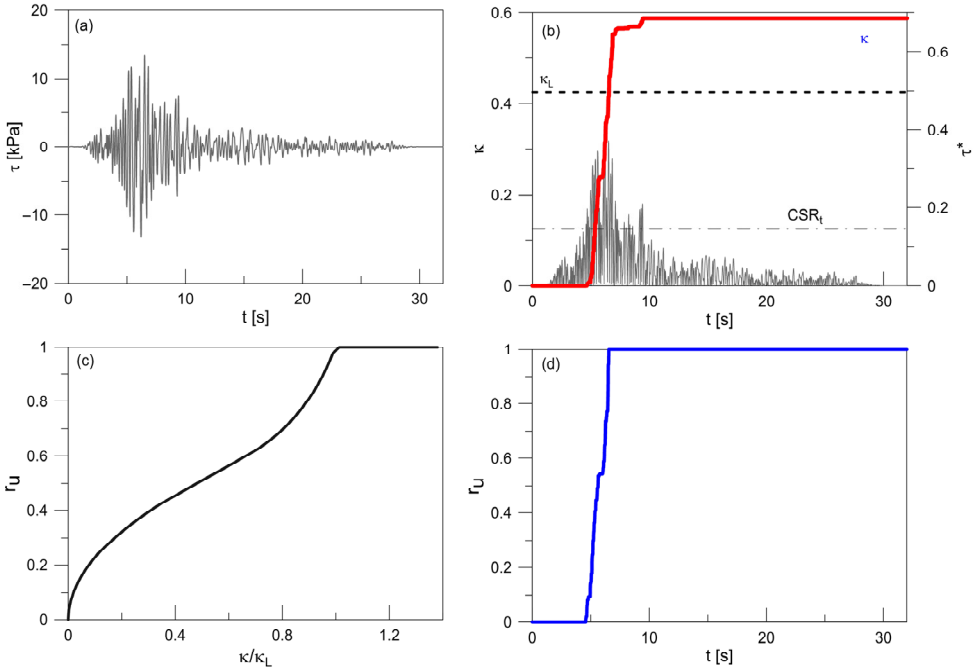


Figure A2. Simplified method: time histories of (**a**) shear stress at 3 m depth; (**b**) normalized shear stress ratio and damage parameter; (**c**) excess pore pressure ratio vs. normalized damage parameter, and (**d**) predicted excess pore pressure ratio time history.

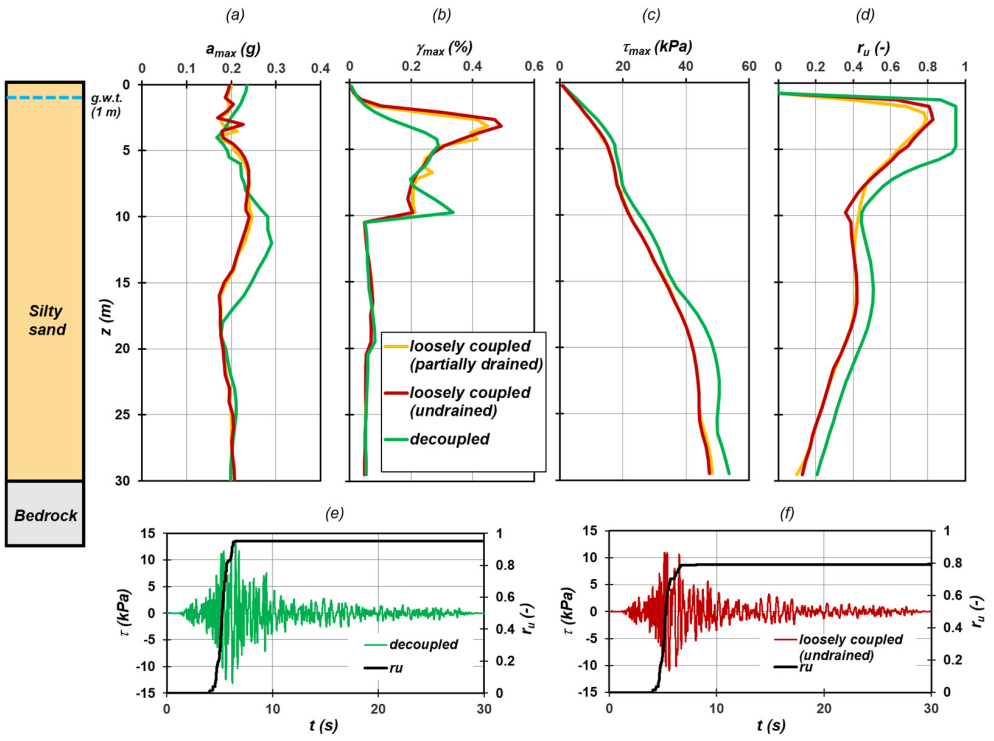


Figure A3. Profiles of maximum (**a**) acceleration, (**b**) shear strain, (**c**) shear stress, (**d**) pore pressure ratio as results of total (decoupled) and effective stress (loosely coupled) dynamic analyses. Shear stress and pore pressure ratio vs. time at 3 m depth from (**e**) decoupled (in green) and (**f**) loosely coupled analysis (in red). Modified after [84].

Appendix A.3. Example Application for Rigorous Methods

Chiaradonna et al. [114] performed numerical simulations to analyze the response of a well-graded gravelly soil using two distinct approaches for effective stress analysis. The simulation employed the PM4Sand [97] constitutive model within the FLAC [115] numerical platform for the advanced fully coupled analysis, and the PWP model developed by Chiaradonna et al. [44], implemented in the SCOSSA [84] code, for the loosely coupled analysis. The boundary value problem examined was the well-instrumented vertical array at Port Island, Japan, which was subjected to the 1995 Kobe earthquake. Calibration of both constitutive models was conducted using data obtained from cyclic and dynamic laboratory tests. Details about the input data of the numerical simulations can be found in [114].

The effective stress analysis results are presented in Figure A4, displaying the time history and response spectrum for the NS acceleration component of the 1995 Kobe earthquake as recorded at Port Island vertical array, which are subsequently compared against the recorded data. The computed spectral ordinates for the NS component were found to be lower than the recorded values in the 0.2 to 3 s period range when using the SCOSSA code. Conversely, simulations performed with FLAC overestimated the peak ground acceleration (PGA) and the spectral accelerations for periods less than 1 s. This trend for periods under 1 s aligns with observations from simulations reported by Ziotopoulou [116]. A detailed view of the time histories between 10 s and 40 s confirms that the simulated accelerations maintain phase with the recorded data (Figure A4b). The adopted liquefaction strength for the Masado soil led to the triggering of the excess pressure build-up for approximately 13 s.

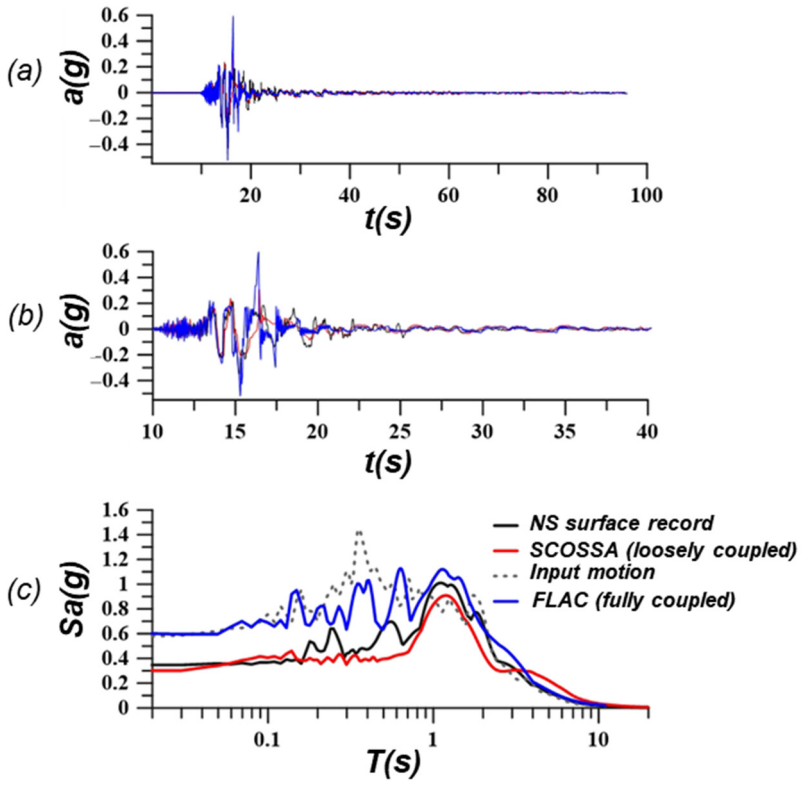


Figure A4. Comparison between effective stress analyses performed with approximate (SCOSSA) and rigorous (FLAC) methods: comparison for the 1995 Kobe earthquake (NS component) between recorded and simulated (**a**) time histories with (**b**) detail between 10 and 40 s and (**c**) 5% damped acceleration response spectra (modified after [114]).

References

1. Doi, I.; Kamai, T. Relationship between earthquake-induced excess pore water pressure and strong ground motion observed in a monitored fill slope. *Eng. Geol.* **2020**, *266*, 105391. [CrossRef]
2. Kamura, A.; Kikumoto, M.; Unno, T.; Matsumaru, T.; Yoshida, S. Monitoring excess pore water pressure during seismic events to assess liquefaction potential in reclaimed land. *Jpn. Geotech. Soc. Spec. Publ.* **2024**, *10*, 546–551. [CrossRef]
3. Jin, D.; Wang, W.; Wei, W.; Liu, W.; Wang, B.; Lu, X. Impact shaking test on excess pore pressure development and water film generation in layered sands. *Soil. Dyn. Earthq. Eng.* **2024**, *184*, 108826. [CrossRef]
4. Özener, P.T.; Özaydin, K.; Berilgen, M. Numerical and physical modeling of liquefaction mechanisms in layered sands. In *Geotechnical Earthquake Engineering and Soil Dynamics IV*; ASCE: Reston, VA, USA, 2008; pp. 1–12.
5. Ecemis, N. Experimental and numerical modeling on the liquefaction potential and ground settlement of silt-interlayered stratified sands. *Soil. Dyn. Earthq. Eng.* **2021**, *144*, 106691. [CrossRef]
6. Dashti, S.; Bray, J.D.; Pestana, J.M.; Riemer, M.; Wilson, D. Centrifuge Testing to Evaluate and Mitigate Liquefaction-Induced Building Settlement Mechanisms. *J. Geotech. Geoenviron. Eng.* **2010**, *136*, 918–929. [CrossRef]
7. Dashti, S.; Bray, J.D.; Pestana, J.M.; Riemer, M.; Wilson, D. Mechanisms of Seismically Induced Settlement of Buildings with Shallow Foundations on Liquefiable Soil. *J. Geotech. Geoenviron. Eng.* **2010**, *136*, 151–164. [CrossRef]
8. Bertalot, D.; Brennan, A.J. Influence of initial stress distribution on liquefaction-induced settlement of shallow foundations. *Géotechnique* **2015**, *65*, 418–428. [CrossRef]
9. Bullock, Z.; Karimi, Z.; Dashti, S.; Porter, K.; Liel, A.B.; Franke, K.W. A physics-informed semi-empirical probabilistic model for the settlement of shallow-founded structures on liquefiable ground. *Géotechnique* **2018**, *69*, 406–419. [CrossRef]
10. Adamidis, O.; Madabhushi, S.P.G. Experimental investigation of drainage during earthquake-induced liquefaction. *Géotechnique* **2018**, *68*, 655–665. [CrossRef]
11. Kuo, Y.S.; Chong, K.J.; Tseng, Y.H.; Hsu, H.T. Excess pore water pressure response of soil inside the mini bucket embedded in saturated soil under seismic loading. *Soil. Dyn. Earthq. Eng.* **2024**, *182*, 108751. [CrossRef]
12. Adamidis, O.; Madabhushi, G.S.P. Post-liquefaction reconsolidation of sand. *Proc. R. Soc. A Math. Phys. Eng. Sci.* **2016**, *472*, 20150745. [CrossRef]
13. Darby, K.M.; Boulanger, R.W.; DeJong, J.T. Effect of partial drainage on cyclic strengths of saturated sands in dynamic centrifuge tests. *J. Geotech. Geoenviron. Eng.* **2019**, *145*, 4019089. [CrossRef]
14. Darby, K.M.; Boulanger, R.W.; DeJong, J.T.; Bronner, J.D. Progressive Changes in Liquefaction and Cone Penetration Resistance across Multiple Shaking Events in Centrifuge Tests. *J. Geotech. Geoenviron. Eng.* **2019**, *145*, 04018112. [CrossRef]
15. Ghazy, M.E.; Abdoun, T.; Dobry, R.; El-Sekelly, W. Centrifuge modeling-of-models investigation on earthquake-induced excess pore pressure behavior of silty sand. *Soil. Dyn. Earthq. Eng.* **2024**, *185*, 108906. [CrossRef]
16. Sinha, S.K.; Ziotopoulou, K.; Kutter, B.L. Effects of excess pore pressure redistribution in liquefiable layers. *J. Geotech. Geoenviron. Eng.* **2024**, *150*, 4024014. [CrossRef]
17. Ma, H.-L.; Feng, X.-L.; Liu, L.-L.; Zhang, A.; Wang, D. Changes in the effective absolute permeability of hydrate-bearing sands during isotropic loading and unloading. *Pet. Sci.* **2025**, *in press*. [CrossRef]
18. Cubrinovski, M.; Rhodes, A.; Ntritsos, N.; Van Ballegooy, S. System response of liquefiable deposits. *Soil Dyn. Earthq. Eng.* **2018**, *124*, 212–229. [CrossRef]
19. Choi, Y.; Kumar, K. A machine learning approach to predicting pore pressure response in liquefiable sands under cyclic loading. In *Geo-Congress 2023*; ASCE: Reston, VA, USA, 2023; pp. 202–210.
20. Biondi, G. Instabilità Sismica Dei Pendii Sabbiosi Causata da Incrementi di Pressione Interstiziale. Ph.D. Thesis, University of Catania, Catania, Italy, 2002.
21. Seed, H.B.; Martin, P.P.; Lysmer, J. Pore-water pressure changes during soil liquefaction. *J. Geotech. Eng. Div.* **1976**, *102*, 323–346. [CrossRef]
22. Seed, H.B.; Booker, J.R. Stabilization of potentially liquefiable sand deposits using gravel drains. *J. Geotech. Eng. Div.* **1977**, *103*, 757–768. [CrossRef]
23. Fardis, M.N.; Veneziano, D. Statistical analysis of sand liquefaction. *J. Geotech. Eng. Div.* **1981**, *107*, 1361–1377. [CrossRef]
24. Chang, C.S.; Kuo, C.L.; Selig, E.T. Pore pressure development during cyclic loading. *J. Geotech. Eng.* **1983**, *109*, 103–107. [CrossRef]
25. Pierce, W.G. *Constitutive Relations for Saturated Sand Under Undrained Cyclic Loading (Pore Pressure, Plasticity)*; Rensselaer Polytechnic Institute: Troy, NY, USA, 1985.
26. Mitchell, R.J.; Dubin, B.I. Pore pressure generation and dissipation in dense sands under cyclic loading. *Can. Geotech. J.* **1986**, *23*, 393–398. [CrossRef]
27. Egglezos, D.N.; Bouckovalas, G.D. Analytical relationships for earthquake induced pore pressure in sand, clay and silt. In Proceedings of the 11th European Conference on Earthquake Engineering, Paris, France, 6–11 September 1998.
28. Martin, G.R.; Seed, H.B.; Finn, W.D.L. Fundamentals of liquefaction under cyclic loading. *J. Geotech. Eng. Div.* **1975**, *101*, 423–438. [CrossRef]

29. Nemat-Nasser, S.; Shokooh, A. A unified approach to densification and liquefaction of cohesionless sand in cyclic shearing. *Can. Geotech. J.* **1979**, *16*, 659–678. [CrossRef]
30. Tsatsanifos, C.P.; Sarma, S.K. Pore pressure rise during cyclic loading of sands. *J. Geotech. Eng. Div.* **1982**, *108*, 315–319. [CrossRef]
31. Booker, J.R.; Rahman, M.S.; Seed, H.B. *GADFLEA: A Computer Program for the Analysis of Pore Pressure Generation and Dissipation During Cyclic or Earthquake Loading*; Earthquake Engineering Research Center, California University: Berkeley, CA, USA, 1976.
32. Pan, K.; Yang, Z.X. Effects of initial static shear on cyclic resistance and pore pressure generation of saturated sand. *Acta Geotech.* **2018**, *13*, 473–487. [CrossRef]
33. Seed, H.B. *Representation of Irregular Stress Time Histories by Equivalent Uniform Stress Series in Liquefaction Analyses*; College of Engineering, University of California: Berkeley, CA, USA, 1975.
34. Annaki, M.; Lee, K.L. Equivalent uniform cycle concept for soil dynamics. *J. Geotech. Eng. Div.* **1977**, *103*, 549–564. [CrossRef]
35. Liu, A.H.; Stewart, J.P.; Abrahamson, N.A.; Moriwaki, Y. Equivalent number of uniform stress cycles for soil liquefaction analysis. *J. Geotech. Geoenviron. Eng.* **2001**, *127*, 1017–1026. [CrossRef]
36. Green, R.A.; Terri, G.A. Number of equivalent cycles concept for liquefaction evaluations—Revisited. *J. Geotech. Geoenviron. Eng.* **2005**, *131*, 477–488. [CrossRef]
37. Keshty, Y.; Carey, T.J. Optimizing Magnitude Scaling Relationships in Simplified Liquefaction Triggering Procedures Using Ground Motion Intensity Measures. *J. Geotech. Geoenviron. Eng.* **2025**, *151*, 4025119. [CrossRef]
38. Biondi, G.; Cascone, E.; Di Filippo, G. Affidabilità di alcune correlazioni empiriche per la stima del numero di cicli di carico equivalente. *Riv. Ital. Geotec.* **2012**, *46*, 9–39.
39. Hashash, Y.; Phillips, C.; Groholski, D.R. Recent advances in non-linear site response analysis. In Proceedings of the 5th International Conference on Recent Advances in Geotechnical Earthquake Engineering and Soil Dynamics, San Diego, CA, USA, 24–29 May 2010.
40. Dobry, R.; Pierce, W.G.; Dyvik, R.; Thomas, G.E.; Ladd, R.S. *Pore Pressure Model for Cyclic Straining of Sand*; Rensselaer Polytech Institute: Troy, NY, USA, 1985.
41. Youd, T.L. Compaction of sands by repeated shear straining. *J. Soil. Mech. Found. Div.* **1972**, *98*, 709–725. [CrossRef]
42. Green, R.A.; Mitchell, J.K.; Polito, C.P. An energy-based excess pore pressure generation model for cohesionless soils. In *Proceedings of the John Booker Memorial Symposium, Sidney Australia*; AA Balkema Publishers: Rotterdam, The Netherlands, 2000.
43. Chen, G.; Zhao, D.; Chen, W.; Juang, C.H. Excess pore-water pressure generation in cyclic undrained testing. *J. Geotech. Geoenviron. Eng.* **2019**, *145*, 4019022. [CrossRef]
44. Chiaradonna, A.; Tropeano, G.; d'Onofrio, A.; Silvestri, F. A Simplified Method for Pore Pressure Buildup Prediction: From Laboratory Cyclic Tests to the 1D Soil Response Analysis in Effective Stress Conditions. *Procedia Eng.* **2016**, *158*, 302–307. [CrossRef]
45. Chiaradonna, A.; Tropeano, G.; d'Onofrio, A.; Silvestri, F. Development of a simplified model for pore water pressure build-up induced by cyclic loading. *Bull. Earthq. Eng.* **2018**, *16*, 3627–3652. [CrossRef]
46. Park, T.; Park, D.; Ahn, J.K. Pore pressure model based on accumulated stress. *Bull. Earthq. Eng.* **2015**, *13*, 1913–1926. [CrossRef]
47. Chiaradonna, A.; Flora, A.; d'Onofrio, A.; Bilotta, E. A pore water pressure model calibration based on in-situ test results. *Soils Found.* **2020**, *60*, 327–341. [CrossRef]
48. Beaty, M.H.; Byrne, P.M. UBCSAND Constitutive Model Version 904aR. Documentation Report: UBCSAND Constitutive Model on Itasca UDM Web Site. Documentation Report. 2011; 69(3), 27. Available online: https://www.researchgate.net/profile/Dinesh-Natarajan-2/post/Anyone_have_UBCSand_dll_in_FLAC2D_version_7/attachment/5b5753474cde265cb6513b51/AS:651955059822602@1532449607724/download/UBCSand.zip (accessed on 23 January 2026).
49. Elgamal, A.; Yang, Z.; Parra, E. Computational modeling of cyclic mobility and post liquefaction site response. *Soil. Dyn. Earthq. Eng.* **2002**, *22*, 259–271. [CrossRef]
50. Dafalias, Y.F.; Manzari, M.T. Simple plasticity sand model accounting for fabric change effects. *J. Eng. Mech.* **2004**, *130*, 622–634. [CrossRef]
51. Boulanger, R.; Ziotopoulou, K. *PM4Sand (Version 2): A Sand Plasticity Model for Earthquake Engineering Applications*; UCD/CGM-12, 1; Center for Geotechnical Modeling, University of California: Davis, CA, USA, 2012.
52. Dobry, R.; Ladd, R.S.; Yokel, F.Y.; Chung, R.M.; Powell, D. *Prediction of Pore Water Pressure Buildup and Liquefaction of Sands During Earthquakes by the Cyclic Strain Method: Building Science Series*; National Bureau of Standards: Washington, DC, USA, 1982.
53. de Cristofaro, M.; Olivares, L.; Orense, R.P.; Asadi, M.S.; Netti, N. Liquefaction of Volcanic Soils: Undrained Behavior under Monotonic and Cyclic Loading. *J. Geotech. Geoenviron. Eng.* **2022**, *148*, 04021176. [CrossRef]
54. Scott, R.F. *Principles of Soil Mechanics*; Addison-Wesley: Boston, MA, USA, 1963.
55. Lambe, T.W.; Whitman, R.V. *Soil Mechanics SI Version*; John Wiley & Sons: Hoboken, NJ, USA, 2008.
56. Polito, C.P.; Green, R.A.; Lee, J. Pore Pressure Generation Models for Sands and Silty Soils Subjected to Cyclic Loading. *J. Geotech. Geoenviron. Eng.* **2008**, *134*, 1490–1500. [CrossRef]

57. Ramirez, J.; Barrero, A.R.; Chen, L.; Dashti, S.; Ghofrani, A.; Taiebat, M.; Arduino, P. Supplemental data. Site Response in a Layered Liquefiable Deposit: Evaluation of Different Numerical Tools and Methodologies with Centrifuge Experimental Results. *J. Geotech. Geoenviron. Eng.* **2018**, *144*, 04018073. [CrossRef]
58. Boccieri, G.; Gaudio, D.; Conti, R. An uncoupled approach for estimating seismic-induced pore water pressures in liquefiable sandy soils. *Comput. Geotech.* **2024**, *170*, 106266. [CrossRef]
59. Matasovic, N.; Hashash, Y.M.A. *Practices and Procedures for Site-Specific Evaluations of Earthquake Ground Motions*; National Academies of Sciences and Medicine: Washington, DC, USA, 2012.
60. Dobry, R.; El-Sekelly, W.; Abdoun, T. Calibration of non-linear effective stress code for seismic analysis of excess pore pressures and liquefaction in the free field. *Soil. Dyn. Earthq. Eng.* **2018**, *107*, 374–389. [CrossRef]
61. He, H.; Miao, Y.; Wang, S. Reproducing nonlinear ground response and pore pressure variations using in-situ soil properties. *Soil. Dyn. Earthq. Eng.* **2025**, *194*, 109380. [CrossRef]
62. Matasović, N.; Vucetic, M. Cyclic characterization of liquefiable sands. *J. Geotech. Eng.* **1993**, *119*, 1805–1822. [CrossRef]
63. Montoya-Noguera, S.; Lopez-Caballero, F. Effect of coupling excess pore pressure and deformation on nonlinear seismic soil response. *Acta Geotech.* **2016**, *11*, 191–207. [CrossRef]
64. Chen, G.; Wang, Y.; Zhao, D.; Zhao, K.; Yang, J. A new effective stress method for nonlinear site response analyses. *Earthq. Eng. Struct. Dyn.* **2021**, *50*, 1595–1611. [CrossRef]
65. Castelli, F.; Grasso, S.; Lentini, V.; Sammito, M. Calibration of the UBC3D-PLM soil model from Dilatometer Marchetti Test (DMT) for the liquefaction behaviour and cyclic resistance ratio (CRR) of sandy soils. *Soil. Dyn. Earthq. Eng.* **2024**, *187*, 109002. [CrossRef]
66. Seed, H.B.; Idriss, I.M. Simplified procedure for evaluating soil liquefaction potential. *J. Soil. Mech. Found. Div.* **1971**, *97*, 1249–1273. [CrossRef]
67. Committee on State of the Art and Practice in Earthquake Induced Soil Liquefaction Assessment, Board on Earth Sciences and Resources, Division on Earth and Life Studies, National Academies of Sciences, Engineering, and Medicine. *State of the Art and Practice in the Assessment of Earthquake-Induced Soil Liquefaction and Its Consequences*; National Academies Press: Washington, DC, USA, 2016.
68. Boulanger, R.W.; Idriss, I.M. *CPT and SPT Based Liquefaction Triggering Procedures*; UCD/CGM-14 1; University of California: Davis, CA, USA, 2014.
69. Idriss, I.M.; Boulanger, R.W. *Soil Liquefaction During Earthquakes*; Earthquake Engineering Research Institute: Oakland, CA, USA, 2008.
70. Robertson, P.K.; Wride, C.E. Evaluating cyclic liquefaction potential using the cone penetration test. *Can. Geotech. J.* **1998**, *35*, 442–459. [CrossRef]
71. Olson, S.M.; Mei, X.; Hashash, Y.M.A. Nonlinear site response analysis with pore-water pressure generation for liquefaction triggering evaluation. *J. Geotech. Geoenviron. Eng.* **2020**, *146*, 4019128. [CrossRef]
72. NTC. *Aggiornamento Delle Norme Tecniche per le Costruzioni*; Official Journal of the Italian Republic: Rome, Italy, 2018.
73. Chiaradonna, A.; Monaco, P. DMT-based liquefaction triggering procedure accounting for the fines content effect. *Soil. Dyn. Earthq. Eng.* **2025**, *199*, 109668. [CrossRef]
74. Andrus, R.D.; Stokoe, K.H., II. Liquefaction resistance of soils from shear-wave velocity. *J. Geotech. Geoenviron. Eng.* **2000**, *126*, 1015–1025. [CrossRef]
75. Kayen, R.E.; Mitchell, J.K.; Seed, R.B.; Lodge, A.; Nishio, S.Y.; Coutinho, R. Evaluation of SPT-, CPT-, and shear wave-based methods for liquefaction potential assessment using Loma Prieta data. In *Technical Report NCEER*; US National Center for Earthquake Engineering Research: Buffalo, NY, USA, 1992; pp. 177–204.
76. Castro, G. Liquefaction and cyclic mobility of saturated sands. *J. Geotech. Eng. Div.* **1975**, *101*, 551–569. [CrossRef]
77. Kramer, S.L. *Geotechnical Earthquake Engineering*; Pearson Education India: Bengaluru, India, 1996.
78. Kramer, S.L.; Stewart, J.P. *Geotechnical Earthquake Engineering*; CRC Press: Boca Raton, FL, USA, 2024.
79. Iwasaki, T.; Arakawa, T.; Tokida, K. Simplified Procedures for Assesing Soil Liquefaction During Earthquakes. *Soil. Dyn. Earthq. Eng.* **1984**, *3*, 49–58.
80. Marcuson, W.F., III; Hynes, M.E.; Franklin, A.G. Evaluation and use of residual strength in seismic safety analysis of embankments. *Earthq. Spectra* **1990**, *6*, 529–572. [CrossRef]
81. Chiaradonna, A.; Flora, A. On the estimate of seismically induced pore-water pressure increments before liquefaction. *Geotech. Lett.* **2020**, *10*, 128–134. [CrossRef]
82. Chiaradonna, A.; Monaco, P.; Karakan, E.; Lanzo, G.; Sezer, A.; Karray, M. Geotechnical Assessment of the Pore Water Pressure Build-Up in Izmir During the October 30, 2020, Samos Earthquake. In Proceedings of the International Conference on Natural Hazards and Infrastructure, Athens, Greece, 5–7 July 2022.
83. Chiaradonna, A. Valutazione del Potenziale di liquefazione dei terreni. Metodi di analisi e applicazioni. In *Collection of Books: Argomenti di Ingegneria Geotecnica 32*; Hevelius Edizioni: Benevento, Italy, 2020; 150p, ISBN 978-88-86977-97-5. (In Italian)

84. Tropeano, G.; Chiaradonna, A.; d'Onofrio, A.; Silvestri, F. A Numerical Model for Non-Linear Coupled Analysis on Seismic Response of Liquefiable Soils. *Comput. Geotech.* **2019**, *105*, 211–227. [CrossRef]
85. Minarelli, L.; Amoroso, S.; Civico, R.; De Martini, P.M.; Lugli, S.; Martelli, L.; Molisso, F.; Rollins, K.M.; Salocchi, A.; Stefani, M.; et al. Liquefied sites of the 2012 Emilia earthquake: A comprehensive database of the geological and geotechnical features (Quaternary alluvial Po plain, Italy). *Bull. Earthq. Eng.* **2022**, *20*, 3659–3697. [CrossRef]
86. Flora, A.; Bilotta, E.; Chiaradonna, A.; Lirer, S.; Mele, L.; Pingue, L. A field trial to test the efficiency of induced partial saturation and horizontal drains to mitigate the susceptibility of soils to liquefaction. *Bull. Earthq. Eng.* **2021**, *19*, 3835–3864. [CrossRef]
87. Flora, A.; Chiaradonna, A.; Bilotta, E.; Fasano, G.; Mele, L.; Lirer, S.; Pingue, L.; Fanti, F. Field tests to assess the effectiveness of ground improvement for liquefaction mitigation. In *Earthquake Geotechnical Engineering for Protection and Development of Environment and Constructions*; CRC Press: Boca Raton, FL, USA, 2019; pp. 740–752.
88. Chiaradonna, A.; Lirer, S.; Flora, A. A liquefaction potential integral index based on pore pressure build-up. *Eng. Geol.* **2020**, *272*, 105620. [CrossRef]
89. Pacor, F.; Paolucci, R.; Luzi, L.; Sabetta, F.; Spinelli, A.; Gorini, A.; Nicoletti, M.; Marcucci, S.; Filippi, L.; Dolce, M. Overview of the Italian strong motion database ITACA 1.0. *Bull. Earthq. Eng.* **2011**, *9*, 1723–1739. [CrossRef]
90. Kottke, A.R.; Wang, X.; Rathje, E.M. *Strata Technical Manual*; Pacific Earthquake Engineering Research Center: Berkeley, CA, USA, 2018.
91. Meletti, C.; Montaldo, V.; Stucchi, M.; Martinelli, F. *Database Della Pericolosità Sismica MPS04*; Istituto Nazionale di Geofisica e Vulcanologia (INGV): Roma, Italy, 2006.
92. Stucchi, M.; Meletti, C.; Montaldo, V.; Crowley, H.; Calvi, G.M.; Boschi, E. Seismic hazard assessment (2003–2009) for the Italian building code. *Bull. Seismol. Soc. Am.* **2011**, *101*, 1885–1911. [CrossRef]
93. Tonni, L.; Gottardi, G.; Amoroso, S.; Bardotti, R.; Bonzi, L.; Chiaradonna, A.; d'Onofrio, A.; Fioravante, V.; Ghinelli, A.; Giretti, D.; et al. Analisi dei fenomeni deformativi indotti dalla sequenza sismica emiliana del 2012 su un tratto di argine del Canale Diversivo di Burana. *Riv. Ital. Di Geotec.* **2015**, *49*, 28–58.
94. Chiaradonna, A.; Tropeano, G.; d'Onofrio, A.; Silvestri, F. Interpreting the deformation phenomena of a levee damaged during the 2012 Emilia earthquake. *Soil Dyn. Earthq. Eng.* **2019**, *124*, 389–398. [CrossRef]
95. Idriss, I.M. An update to the Seed-Idriss simplified procedure for evaluating liquefaction potential. In *Proceedings: TRB Worshop on New Approaches to Liquefaction*; Pubbl. n. FHWA-RD-99-165; Federal Highway Administration: Washington, DC, USA, 1999.
96. Itasca Consulting Group. An Introduction to FLAC 8 and a Guide to Its Practical Application in Geotechnical Engineering-Online Manual. 2015. Available online: https://itasca-downloads.s3.amazonaws.com/documents/software/manuals/FLAC8Basics.pdf (accessed on 23 January 2026).
97. Boulanger, R.W.; Ziotopoulou, K. *PM4Sand (Version 3.1): A Sand Plasticity Model for Earthquake Engineering Applications; UCD/CGM-17/01*; Center for Geotechnical Modelling, Department of Civil and Environmental Engineering, University of California: Davis, CA, USA, 2017; 108p.
98. Boulanger, R.W.; Ziotopoulou, K. *PM4Silt (Version 1): A Silt Plasticity Model for Earthquake Engineering Applications; Report No. UCD/CGM-18/01; Center for Geotechnical Modelling, Department of Civil and Environmental Engineering*; University of California: Davis, CA, USA, 2018.
99. Hutabarat, D.; Bray, J.D. Effective stress analysis of liquefiable sites to estimate the severity of sediment ejecta. *J. Geotech. Geoenviron. Eng.* **2021**, *147*, 4021024. [CrossRef]
100. Hutabarat, D.; Bray, J.D. Estimating the severity of liquefaction ejecta using the cone penetration test. *J. Geotech. Geoenviron. Eng.* **2022**, *148*, 4021195. [CrossRef]
101. Dhakal, R.; Ntritsos, N.; Cubrinovski, M. Evaluation of liquefaction ejecta potential from case histories and insights from nonlinear dynamic analyses. *J. Geotech. Geoenviron. Eng.* **2026**, *152*, 4025174. [CrossRef]
102. Chiaradonna, A.; d'Onofrio, A.; Bilotta, E. Assessment of post-liquefaction consolidation settlement. *Bull. Earthq. Eng.* **2019**, *17*, 5825–5848. [CrossRef]
103. Cascone, E.; Biondi, G.; Casablanca, O. Influence of earthquake-induced excess pore water pressures on seismic bearing capacity of shallow foundations. In *Earthquake Geotechnical Engineering for Protection and Development of Environment and Constructions*; CRC Press: Boca Raton, FL, USA, 2019; pp. 566–581.
104. Noda, T.; Yamada, S.; Nonaka, T.; Tashiro, M. Study on the pore water pressure dissipation method as a liquefaction countermeasure using soil–water coupled finite deformation analysis equipped with a macro-element method. *Soils Found.* **2015**, *55*, 1129–1138. [CrossRef]
105. Chian, S.C.; Du, S. Understanding Excess Pore Water Dissipation in Soil Liquefaction Mitigation. In *Conference on Performance-Based Design in Earthquake. Geotechnical Engineering*; Springer: Berlin/Heidelberg, Germany, 2022; pp. 353–362.
106. Huang, S.; Zhai, S.; Liu, Y.; Liu, C.; Goda, K.; Mou, B. Seismic behavior analysis of the bank slope considering the effect of earthquake-induced excess pore water pressure. *Front. Earth Sci.* **2021**, *9*, 799612. [CrossRef]

107. Hu, J.; Chen, Q.; Liu, H. Relationship between earthquake-induced uplift of rectangular underground structures and the excess pore water pressure ratio in saturated sandy soils. *Tunn. Undergr. Space Technol.* **2018**, *79*, 35–51. [CrossRef]
108. Maurer, B.W.; Green, R.A.; Cubrinovski, M.; Bradley, B.A. Evaluation of the liquefaction potential index for assessing liquefaction hazard in Christchurch, New Zealand. *J. Geotech. Geoenviron. Eng.* **2014**, *140*, 4014032. [CrossRef]
109. Ziotopoulou, K.; Boulanger, R.W. Calibration and implementation of a sand plasticity plane-strain model for earthquake engineering applications. *Soil. Dyn. Earthq. Eng.* **2013**, *53*, 268–280. [CrossRef]
110. Ntritsos, N.; Cubrinovski, M. A CPT-based effective stress analysis procedure for liquefaction assessment. *Soil. Dyn. Earthq. Eng.* **2020**, *131*, 106063. [CrossRef]
111. Merli, A.; Dezi, F.; Tropeano, G.; Chiaradonna, A.; d'Onofrio, A. Site response analysis in effective stress of a coastal area in the North-Western Adriatic region (Italy). In *Earthquake Geotechnical Engineering for Protection and Development of Environment and Constructions*; CRC Press: Boca Raton, FL, USA, 2019; pp. 3893–3900.
112. Banca Dati delle Prove Geognostiche della Regione Emilia-Romagna. Available online: https://servizimoka.regione.emilia-romagna.it/mokaApp/apps/geg/index.html (accessed on 23 January 2026).
113. Porcino, D.; Diano, V. Laboratory study on pore pressure generation and liquefaction of low-plasticity silty sandy soils during the 2012 earthquake in Italy. *J. Geotech. Geoenviron. Eng.* **2016**, *142*, 4016048. [CrossRef]
114. Chiaradonna, A.; Mohammadi, R.; Monaco, P. Simulation of the Seismic Response of a Man-Made Well-Graded Gravel as Recorded by a Vertical Instrumented Array. In *Geo-Congress 2024*; ASCE: Reston, VA, USA, 2024; pp. 132–140.
115. Itasca Consulting Group. *FLAC—Fast Lagrangian Analysis of Continua; User's Guide*; Itasca Consulting Group: Minneapolis, MN, USA, 2021.
116. Ziotopoulou, A. Evaluating model uncertainty against strong motion records at liquefiable sites. In *Masters Abstracts International*; ProQuest: Ann Arbor, MI, USA, 2010.

Disclaimer/Publisher's Note: The statements, opinions and data contained in all publications are solely those of the individual author(s) and contributor(s) and not of MDPI and/or the editor(s). MDPI and/or the editor(s) disclaim responsibility for any injury to people or property resulting from any ideas, methods, instructions or products referred to in the content.